

*Regular Article***Practical considerations for feature assignment in high-speed AFM of live cell membranes**Damien Hall^{1,2}, Adam S. Foster^{1,2}¹ WPI Nano Life Science Institute, Kanazawa University, Kanazawa, Ishikawa 920-1164, Japan² Department of Applied Physics, Aalto University, FI-00076 Aalto, Finland

Received September 27, 2021; Accepted April 13, 2022;

Released online in J-STAGE as advance publication April 15, 2022

Edited by Yasushi Sako

High speed atomic force microscopy (HS-AFM) is, in principle, capable of yielding nanometer level detail about the surface of static structures. However, for highly dynamic samples HS-AFM may struggle with the correct feature assignment both within and between frames. Feature assignment in HS-AFM is dependent on (i) the intrinsic sampling rate, and (ii) the rate of internal redistribution of the sample. Whilst the first quantity (the sampling rate) is defined by the device parameters, the second quantity is frequently unknown, and is often the desired target of the measurement. This work examines how, even in the absence of gross cell morphological change, the rapid dynamics of living cell membranes, may impose an upper spatial limit to the frame-to-frame assignment of cell micro-topography and other related properties (such as local elasticity) whose motion may be described stochastically. Such a practical maximum may prove useful in the setup of HS-AFM experiments involving dynamic surfaces thereby facilitating selection of the most parsimonious relationship between observation size, image pixilation and sampling rates. To assist with performing the described calculations a graphical user interface-based software package called HS-AFM UGOKU is made freely available.

Key words: high-speed atomic force microscopy, experimental optimization, live cell membranes, dynamic surfaces**◀ Significance ▶**

This work examines how the rapid local dynamics of living cell membranes may complicate high-speed atomic force microscopy measurements. It also provides methods for deconvolution of these difficulties, both at the experimental design and post experimental analysis stages.

Introduction

When analyzing image time series of a cell membrane acquired using some microscopy technique, a common question arises that relates to feature assignment i.e. how do the features observed at one time-point relate to those recorded at another [1,2] (Fig. 1). Although this question has been extensively considered in the field of single particle tracking conducted using optical microscope procedures [3-5], the same type of problem has been less-well investigated in atomic force microscopy (AFM) measurements [6-8]. As continual scientific and technological developments produce ever faster AFM scan rates [9, 10] the potential use of AFM devices to track the motion of slowly moving diffusible components in the cell membrane, such as protein receptors and membrane channels [11], is becoming tantalizingly extant. In preparation

Corresponding authors: Damien Hall, WPI Nano Life Science Institute, Bldg. 58, Kanazawa University, Kakumamachi, Kanazawa, Ishikawa 920-1164, Japan. ORCID iD: <https://orcid.org/0000-0003-1538-7618>, e-mail: hall.damien@staff.kanazawa-u.ac.jp; damienhall30@gmail.com; Adam S. Foster, Department of Applied Physics, Aalto University, Puumiehenkuja 2, 02150 Espoo, FI-00076 Aalto, Finland. ORCID iD: <https://orcid.org/0000-0001-5371-5905>, e-mail: adam.foster@aalto.fi

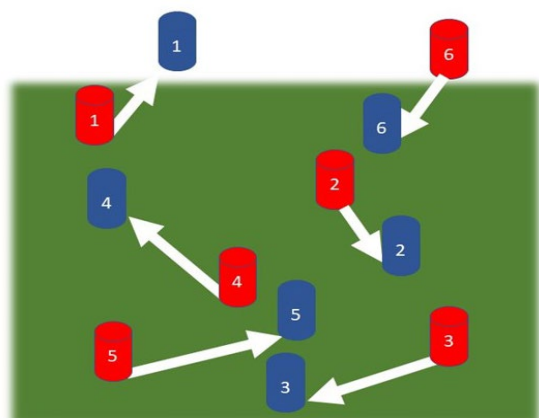


Figure 1 Schematic of the general principle of feature assignment applied to a dynamic cell membrane surface: A subset of membrane surface features (1-6) exist within the scan imaged area and are recorded at a time t_1 (indicated in red). The same region of membrane surface is then recorded at a later time t_2 , after which the surface features have moved, with their new position shown in blue. Feature assignment involves identifying and mapping the identity of the specific features between frames.

tailored AFM instrumentation, developed for measuring samples immersed in liquid, operate in the AM mode (also called tapping mode) [16]. Whilst a comprehensive discussion of all of the technical aspects of AFM is beyond the scope of the current work, we present here a number of core points that will prove useful for introducing the present topic of study (Fig. 2b). Important parameters include the maximum side lengths of the x and y axes defining the scanned image area [x_{max} , y_{max}], the effective z-axis tip oscillation frequency and tip amplitude pairing, [f , A] and the linear tip scan rates in the x (lateral) and y (vertical) directions, [v_x , v_y]. When the tip is in contact with the surface, the x linear scan rate, together with the z-axis oscillation frequency, determines the effective minimum lateral line sampling distance, $x_{min} = (v_x/f)$. Although not absolutely required, for reasons of simplicity, in this work we set the minimum vertical line sampling distance equal to its lateral counterpart i.e. $y_{min} = x_{min}$.

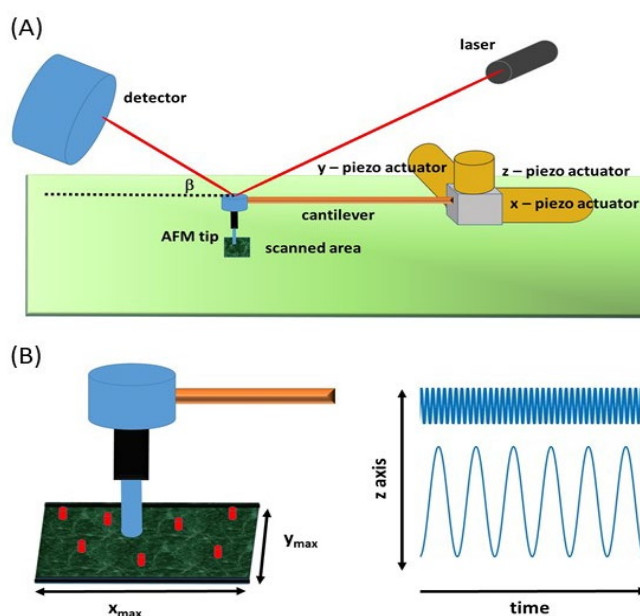
Figure 2 Schematic showing important aspects of the HS-AFM experiment. (A) Physical components of an AFM force gauge – include the AFM tip, an oscillating cantilever arm, piezoelectric actuators (responsible for x,y,z-based translation), and a laser and photodetector for inferring tip height/lateral resistance via the recorded laser deflection angle β . (B) AFM tip scanning an area that contains mobile components – The scanned image area, defined by a maximum x and y range, contains an arbitrary number of mobile components. In the simplest case the AFM is translated laterally and vertically at velocities v_x and v_y whilst oscillating along the z-axis at some frequency f , amplitude, A pairing governed by the cantilever characteristics (two types of such pairing are shown – a high frequency/low amplitude oscillation and a low frequency/high amplitude oscillation).

for this potentially game-changing technological improvement in the high-speed atomic force microscopy (HS-AFM) technique, here we focus on the question of what biological and instrumental factors would affect the feature assignment of mobile cell membrane components observed using HS-AFM [12,13] in a manner that will lead to improved experimental design. However, prior to discussing feature assignment in HS-AFM experiments we introduce some operational aspects of the AFM technique that will facilitate the principal discussion.

Theory and Results

Preliminary Description of AFM

At its core, an AFM is a translatable force gauge equipped with a nanometer-diameter sensing probe [14-16]. The probe, also known as the AFM tip, can be brought into contact with the surface, with the degree of applied force able to be regulated via a feedback control circuit that uses some measurable aspect of the interaction with the sample as input [16,17] (Fig. 2a). The relatively recent development of HS-AFM was made possible through advances in cantilever/tip manufacture and tip/sample spatial control (via use of integrated piezoelectric materials) [12,13]. To enhance sampling rates and the degree of surface coverage, in most modern AFM devices the tip is typically induced to continually oscillate, with the measurement control principles governing the tip/surface interaction based on either amplitude modulation (AM) or frequency modulation (FM) [18]. The vast majority of biologically



Pixilation Within an AFM Image

An important step in any AFM experiment is setting the degree of image pixilation [17,19,20] (Fig. 3). A pixel is the basic unit of information within a two-dimensional digital image that is defined by a rectangle of side-lengths x_{pixel} and y_{pixel} and one or more numerical value(s) representing the positional magnitude of the measured variable(s) [21]. Competing factors based on minimizing image size, maximizing signal to noise ratio, maximizing image resolution and minimizing scan time all play a role in dictating the final values of the adopted pixel dimensions [17,22]. The tension between these different determinants can be best understood by comparing the lateral and vertical pixel dimensions (x_{pixel} , y_{pixel}) against the minimum sampling distance ($x_{\text{min}} = y_{\text{min}}$) and the AFM tip diameter, ϕ (here for simplicity we consider the AFM tip as a right circular cylinder) (Fig. 3a). If we consider the measured variable as the pixel centered surface height, $h_{x,y}$, then we note that when $(x_{\text{pixel}}, y_{\text{pixel}}) > x_{\text{min}}$ the reported pixel value is the average of the numerous internal values obtained at the sampling interval x_{min} (Eqn. 1a – with i and j representing running indices for subpoints within the pixel with N_x and N_y describing the number of subpoints in the x and y directions). For static surfaces, such averaging will yield improvements in the signal to noise ratio for locally non-rough surfaces [20,22,23]. Alternatively, when $(x_{\text{pixel}}, y_{\text{pixel}}) = x_{\text{min}}$ the maximum data driven image pixilation (smallest pixel size possible with maximum number of pixels in image) is achieved such that the reported height is the single measured value at that point (Eqn. 1b).

$$h_{x,y} = \frac{\left(\sum_{i=1}^{N_x} \sum_{j=1}^{N_y} z_{i,j}\right)}{(x_{\text{pixel}}/x_{\text{min}})(y_{\text{pixel}}/y_{\text{min}})} \quad \text{for } (x_{\text{pixel}}, y_{\text{pixel}}) > x_{\text{min}} \quad (1a)$$

$$h_{x,y} = z_{x,y} \quad (x_{\text{pixel}}, y_{\text{pixel}}) = x_{\text{min}} \quad (1b)$$

An important distinction in surface sampling can be made when the minimum sampling distance is considered in relation to the tip diameter. For regimes in which $x_{\text{min}} \leq \phi$ we may say that the surface is ‘continuously’ sampled whereas for the situation $x_{\text{min}} > \phi$ we describe the surface coverage as ‘discontinuously’ sampled. In relation to Eqn. 1 we can set the joint limit of continuous sampling and minimum degree of image pixilation as occurring at the point $x_{\text{min}} = \phi$. At this continuous/discontinuous sampling juncture the lateral image resolution, λ , (in the analysis of static samples) will approximately be equal to the minimum sampling distance i.e. $\lambda \sim \phi$. Neglecting a minor correction for factoring in the feedback control delay, this sampling limit also acts to define the fastest achievable ‘continuous’ lateral scan velocity (Eqn. 2a) which, in turn, defines the fastest continuous vertical scan velocity (Eqn. 2b).

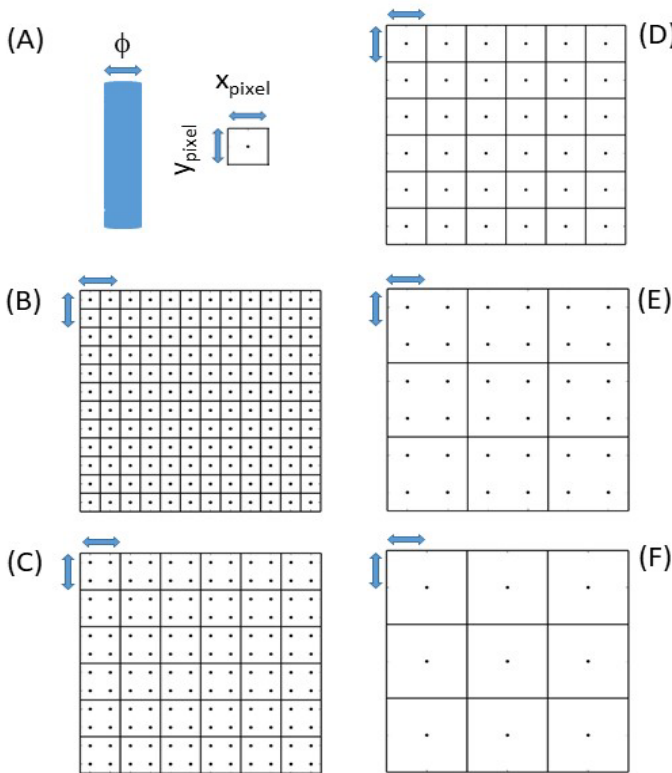


Figure 3 Schematic describing some conventional points of interest for deciding the degree of AFM image pixilation for a static surface in relation to the AFM tip diameter, ϕ . (A) Limit of continuous sampling when pixel dimensions are the same size as the effective tip diameter ($x_{\text{pixel}} = y_{\text{pixel}} = \phi$) (AFM tip shown as a blue cylinder). Different types of continuous spatial pixilation (B-D): (B) Oversampling without averaging when $(x_{\text{pixel}} = x_{\text{min}}) < \phi$ (with minimum spatial signal to noise ratio). (C) Oversampling with averaging ($x_{\text{pixel}} > x_{\text{min}}) \leq \phi$ (to improve the spatial signal to noise ratio). (D) Limit of continuous sampling, $x_{\text{pixel}} = (x_{\text{min}}, \phi)$ (with maximum pixel size, minimum signal to noise ratio, minimum image size and maximum sampling rate). Different types of discontinuous spatial pixilation (E-F): (E) The information in a continuously sampled image can be averaged over a pixel spacing larger than the AFM tip diameter to produce a ‘discontinuous’ pixilation, $x_{\text{pixel}} > (x_{\text{min}}, \phi)$ (where spatial resolution is traded for an increased spatial signal to noise ratio and smaller image size). (F) Discontinuous sampling in which $(x_{\text{pixel}} = x_{\text{min}}) > \phi$ (yielding low resolution and a low signal to noise ratio but a small image size and fast sampling).

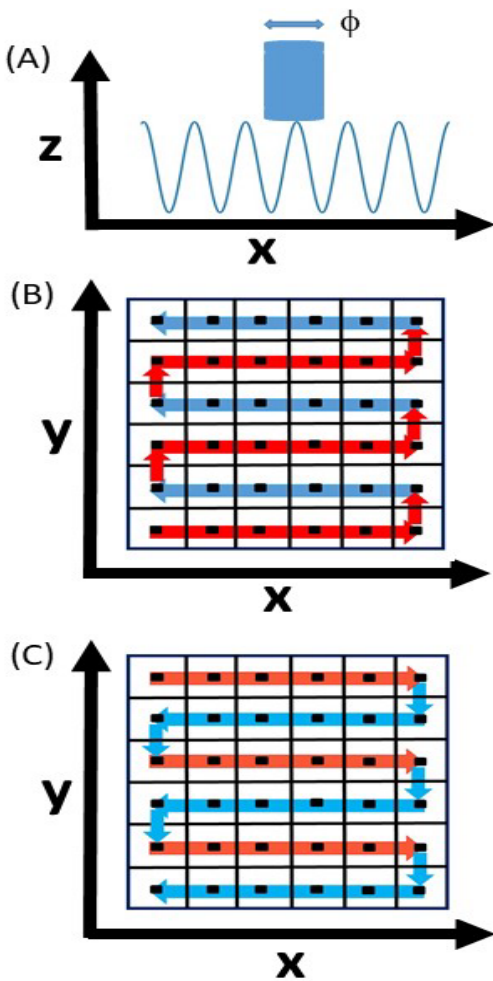
$$(v_x)_{max} = f\phi \tag{2a}$$

$$(v_y)_{max} = \left(\frac{f\phi^2}{x_{max}}\right) \tag{2b}$$

The smallest productive file size that also corresponds to the fastest possible image scanning rate within the continuous sampling regime is given by Eqn. 3.

$$(Image\ Size)_{min} = \frac{(x_{max} y_{max})}{\phi^2} \tag{3}$$

Having raised some of the factors that jointly optimize the fastest possible scan rates, smallest file size and best resolution we now turn to an examination of how the adopted approach for scanning the surface determines the total scanning time. However, we will revisit the topic of pixilation in the discussion, pointing out some important differences between the averaging process for static and dynamic surfaces.



Raster Scanning Patterns

In HS-AFM the surface is typically interrogated by using raster scanning [24]. Calculation of the return rate of the raster scanning tip to its original position requires knowledge of the scanned image dimensions, the linear scanning rate, the pixilation dimensions and definite assignment of a raster pattern. Although more complex scan patterns are available [24-26] (and discussed in Supplementary 2), we concentrate here on the commonly adopted square grid-based raster pattern applied within the just discussed continuous sampling limit, which we operationally define here as ‘continuous raster’.

Continuous Raster

Continuous scanning applies a fast oscillating, small amplitude vibration to the AFM tip [f,A] under conditions defined by Eqn. 2a such that the maximum scanning velocities and minimum pixilation distance are respectively given by $(v_x)_{max} = f\phi$, $(v_y)_{max} = f\phi^2/x_{max}$ and $x_{pixel} = y_{pixel} = \phi$ (note this also implies that the lateral resolution, λ , for static samples, is approximately $\lambda \sim \phi$) (Fig. 4a). Raster scanning follows a classical grid pattern with tip motion tracing successive positive and negative directions along the x axis (Fig. 4b,c) [24]. Step increments on the y axis occur in an initially positive direction, until the maximum of the y value range is met, upon which the y axis step increments then become negative for the return raster journey. Due to the back-and-forth nature of the raster scanning process, the tip return rate, Δt_{ret} , becomes both a function of pixel position, and direction (positive or negative) of the y step increments. Assuming that the x and y line assignment, ℓ_x and ℓ_y , and xy-pixel assignment, $p_{x,y}$, are set as per a Cartesian graph coordinate system with the maximum line range values for the x and y axes given by $\ell_x \in (1, x_{max}/x_{pixel})$ and $\ell_y \in (1, y_{max}/y_{pixel})$, then the time for tip-pixel encounter in the positive, t_{pos} , and negative, t_{neg} , raster scan directions from the respective positive and negative starting positions, are given by Eqn. 4. Other raster patterns are discussed in Supplementary 2.

Figure 4 Schematic showing the basic principles of continuous raster scanning and pixilation in HS-AFM. (A) Spatial XZ-oscillation pattern of AFM tip for ‘continuous’ raster scanning: Continuous raster scanning results from high frequency oscillation under the condition $(v_x/f) \leq \phi$ (where ϕ = diameter of the AFM tip – shown as a blue cylinder, f is the AFM tip cantilever oscillation frequency and v_x is the lateral scan velocity). (B) Positive XY raster scanning pattern and pixilation: Continuous sampling of the surface whereby sequential scanning proceeds quickly in the positive and negative x direction with slow advancement in the positive y direction. (C) Negative XY raster scanning pattern and pixilation: As per B with raster direction reversed. (Red arrows positive direction, blue arrows negative direction).

$$t_{pos}(p_{X,Y}) = \begin{cases} (\ell_X - 1) \left(\frac{x_{pixel}}{v_x} \right) + (\ell_Y - 1) \left(\frac{y_{pixel}}{v_y} \right) & \ell_Y = \text{odd} \\ \left(\frac{x_{max}}{x_{pixel}} - \ell_X \right) \left(\frac{x_{pixel}}{v_x} \right) + (\ell_Y - 1) \left(\frac{y_{pixel}}{v_y} \right) & \ell_Y = \text{even} \end{cases} \quad (4a)$$

$$t_{neg}(p_{X,Y}) = \begin{cases} (\ell_X - 1) \left(\frac{x_{pixel}}{v_x} \right) + \left(\frac{y_{max}}{y_{pixel}} - \ell_Y \right) \left(\frac{y_{pixel}}{v_y} \right) & \ell_Y = \text{even} \\ \left(\frac{x_{max}}{x_{pixel}} - \ell_X \right) \left(\frac{x_{pixel}}{v_x} \right) + \left(\frac{y_{max}}{y_{pixel}} - \ell_Y \right) \left(\frac{y_{pixel}}{v_y} \right) & \ell_Y = \text{odd} \end{cases} \quad (4b)$$

For the sake of creating a characteristic AFM temporal constant we define the time taken to complete one tour of the pixel matrix (from the first to the last pixel) as t_{SCAN} . We note that the shortest possible scan time within the continuous sampling limit is given by Eqn. 5a which for the case of a square scanned image area ($L = x_{max} = y_{max}$) is given by Eqn. 5b.

$$t_{SCAN} = \frac{y_{max}}{\left(\frac{f\phi^2}{x_{max}} \right)} \quad (5a)$$

$$t_{SCAN} = \frac{L^2}{f\phi^2} \quad (5b)$$

We now use this characteristic t_{SCAN} constant to discuss how AFM sampling rates might be usefully compared with the dynamic processes occurring within the cell membrane.

AFM Assignment for Mobile Cell Membranes

The theoretical potential of an AFM device to measure spatially dependent properties at nanometer levels of lateral resolution and sub-nanometer levels of vertical resolution [16,18] has driven interest into its application to cell biology since soon after the time of its invention [27,28]. Non-penetrative measurements of a cell's behavior principally involve the high spatial density recording of relatively soft interactions between the AFM tip and the outer cell membrane [28,29]. However, due to its non-equilibrium nature the cell membrane is a dynamic structure that changes over time [30-36]. In terms of how this change occurs, we make a distinction between (i) relatively large-scale ($\sim 100\text{nm}$) gross morphological changes in membrane shape that occur slowly with a time constant, τ_1 (\sim minutes) [e.g. 31,35,37] and (ii) relatively small-scale (~ 10 nm) changes in the local composition of the two-dimensional membrane fluid, occurring more rapidly with a time constant, τ_2 (\sim milliseconds) [1,38-40]. Although we will define this parameter more carefully in a subsequent section we consider for now that the AFM measurement itself proceeds with a time constant of the order of t_{SCAN} . To a first approximation we compare these different characteristic time constants (τ_1 , τ_2 , t_{SCAN}) to define three disparate dynamic regimes of cell membrane motion with each characterized by a corresponding potential capability to relate information between scans via spatial feature assignment.

Regime 1: ($\tau_2 < \tau_1$) $\ll t_{SCAN} \rightarrow$ Low confidence

Regime 2: $\tau_2 < t_{SCAN} < \tau_1 \rightarrow$ Intermediate confidence

Regime 3: $t_{SCAN} \leq \tau_2 < \tau_1 \rightarrow$ High confidence

In regime 1, the rate of the AFM measurement is slow in comparison to both the large-scale and small-scale changes in the membrane, resulting in low confidence ability to make spatial assignment between observations. In regime 2 the AFM measurement process is considered fast in relation to the large-scale changes in cell membrane structure but slow in relation to the small-scale changes in membrane composition. This level of resolution is sufficient to assign changes in gross morphological structure, such as for those occurring in cell division [41,42], exosome formation [43], pseudopodia/microvilli projections [44,45] and cell membrane reorganization [29,30,32]. However, the rate of AFM measurement is not sufficient to track and identify molecular level changes in plasma membrane components. Within regime 3 the AFM measurement is considered to operate at a rate comparable to, or faster than, the rate of local redistribution of the membrane contents, thereby potentially allowing for assignment of changes observed between scans. Such a relative temporal difference can be effected in practice by either slowing down the rate of internal redistribution of the membrane (e.g. by chemical fixation [33,46,47]) or by speeding up the rate of the AFM measurement [16,31,48].

As HS-AFM technologies have continued to improve the $t_{SCAN} \leq \tau_2$ limit of regime 3 has begun to be approached [16,49,50] such that it is now relevant to investigate the potential for AFM-based assignment of features observed in live

cell membranes. To examine this question we have performed both analytical and numerical calculations of an idealized HS-AFM experiment carried out on a region of an otherwise effectively flat cell membrane surface. The measurable difference in some observable property (e.g. vertical height, Δz) is conserved due to a single type of mobile component, denoted as species q , that is capable of random motion defined by a spatially isotropic two-dimensional diffusion coefficient, D_q (Fig. 1). Throughout this paper we will consider a square scanned area on a cell membrane defined by a side length of $10\mu\text{m}$ and which contains within it at least one q -type molecule that features an observable topographical projection Δz , and which displays mobility characteristics that comport to either a lipid or peripheral membrane protein [38,51,52], an integral membrane protein [38,53] or a clustered domain of both protein and lipid [54,55]. From experimental measurements of diffusion in artificial vesicle systems, it has been shown that lipid and integral membrane proteins typically show a ten-fold difference in their respective mobilities within the phospholipid bilayer ($D_q^\circ \sim [1,10] \mu\text{m}^2\text{s}^{-1}$) [38,53-57]. This relative difference is somewhat extended in real cell membranes, with the range of absolute mobilities for each decreased by a factor of ten to one-hundred, ($D_q^{\text{real}} \sim [0.01,1] \mu\text{m}^2\text{s}^{-1}$) [38,58]. Theoretical support for this range of experimentally observed values is also given by the Saffman-Delbrück equation (Eqn. 6a) [59,60] which is able to predict the diffusion coefficient of cylindrical rods of radius R_q randomly moving in a continuum two-dimensional fluid of viscosity, η_{2d} , and thickness, H , with the 2d-fluid itself supported in a three-dimensional solvent of viscosity, η_{3d} (with γ denoting the Euler-Mascheroni constant approximately given by 0.5772). Typical values for the two-dimensional membrane viscosity and the three-dimensional solution viscosity at 37°C are $\eta_{2d} = 2.7 \times 10^{-1} \text{kgm}^{-1}\text{s}^{-1}$ and $\eta_{3d} = 0.7 \times 10^{-3} \text{kgm}^{-1}\text{s}^{-1}$ [61]. The Saffman-Delbrück equation can also be extended to predict the diffusion constant of components in membranes that are densely populated by proteins (defined as a fractional membrane area occupation θ), either over a very short time, D_q^S (Eqn. 6b) – with the fractional area occupation averaged over a local area, $\langle\theta\rangle_{\text{local}}$, or a longer time, D_q^L (Eqn. 6c) – with the fractional area occupation averaged over the total area, $\langle\theta\rangle$ [60-63].

$$D_q^\circ = \frac{kT}{4\pi\eta_{2d}H} \left(\log_e \left(\frac{\eta_{2d}H}{\eta_{3d}R_q} \right) - \gamma \right) \quad (6a)$$

$$D_q^S = D_q^\circ \left(1 - 2\langle\theta\rangle_{\text{local}} + \frac{2.8238\langle\theta\rangle_{\text{local}}}{\left(\log_e \left(\frac{\eta_{2d}H}{\eta_{3d}R_q} \right) - \gamma \right)} \right) \text{ for } \langle\theta\rangle_{\text{local}} \leq 0.35 \quad (6b)$$

$$D_q^L = D_q^L (1 - 2.1187\langle\theta\rangle + 1.802\langle\theta\rangle^2 - 1.6304\langle\theta\rangle^3 + 0.9466\langle\theta\rangle^4) \text{ for } \theta \leq 0.7 \quad (6c)$$

An empirical anomalous diffusion relation can be used to fit the transition between D_q^S and D_q^L [62] (Table 1).

Table 1 Reduction in diffusion coefficient, D_q° , of a cylindrical particle existing in the cell membrane as a function of particle radius, and fractional area occupation $\langle\theta\rangle$ or $\langle\theta\rangle_{\text{local}}$

R_q/H	D_q°/D_q° *	$\langle\theta\rangle$ or $\langle\theta\rangle_{\text{local}}$	D_q^S/D_q° **	D_q^L/D_q° ***
0.1	1	0	1	1
0.25	0.87	0.05	0.96	0.90
0.5	0.77	0.1	0.92	0.80
0.75	0.71	0.15	0.88	0.72
1	0.67	0.2	0.84	0.64
2	0.57	0.25	0.81	0.56
3	0.51	0.3	0.77	0.49
4	0.47	0.35	0.73	0.42
5	0.44	0.4		0.36
10	0.34	0.5		0.25
50	0.10	0.6		0.15
100	0.003	0.7		0.07

At 37°C are $\eta_{2d} = 2.7 \times 10^{-1} \text{kgm}^{-1}\text{s}^{-1}$ and $\eta_{3d} = 0.7 \times 10^{-3} \text{kgm}^{-1}\text{s}^{-1}$. Membrane height H set at 5 nm.

Saffman-Delbrück equation (Eqn. 2a [52]) provides respective estimates D_q° for a lipid ($R_q = 0.5\text{nm}$, $H = 2.5\text{nm}$) and a mid-sized membrane protein ($R_q = 2.5\text{nm}$, $H = 5\text{nm}$) in a model lipid bilayer at 37°C as $1.5 \mu\text{m}^2\text{s}^{-1}$ and $0.6 \mu\text{m}^2\text{s}^{-1}$.

* Calculated using the Saffman-Delbrück equation (Eqn. 2a [52]) and normalized with respect to $D_q^\circ \left(\frac{R_q}{H} = 0.1 \right)$.

** Calculated using the equation of Bussell, Koch and Hammer (Eqn. 2b [56]), normalized for $D_q^\circ \left(\frac{R_q}{H} = 0.5 \right)$.

*** Calculated using the equation of Saxton (Eqn.2c [55]).

In the simulations that follow, the scanned image area containing the mobile component is subjected to raster scanning at either a slow, medium or fast scanning speed such that $t_{SCAN} \in (1, 10, 100)$ s. Interpreted through the lens of Eqn. 5 this implies that for a square image scan area of $L = 10\mu\text{m}$, and a typical AFM device setup with a tip size $\phi \in (10, 100)$ nm, the required AFM cantilever tip oscillation frequencies and tip lateral scan velocities will be in the respective ranges, $f \in (100, 1 \times 10^6)$ and $v_x \in (0.01, 10)$ mm/s – values which are compatible with current state of the art HS-AFM devices [36,64]. In a corresponding fashion we bracket a range of diffusion constants relevant to the motion of lipids, proteins and protein complexes within a typical phospholipid cell membrane, sampling from $D_q \in [0.01, 0.1, 1] \mu\text{m}^2\text{s}^{-1}$.

(i.) What Situations are Assignable?

In order to assign the identity of a mobile particle between successive scans we must first examine an even more basic question that relates to defining which types of mobile systems are indeed ‘assignable’ in the time frame of the measurement. During the course of the first scan, the q-type particle will be initially located at some starting position, $\mathbf{r}(t_0) = [x, y]$ that corresponds to a pixel coordinate, $(p_{X,Y})_{start}$. Depending upon both (i) the initial position of the particle within the scanned region of interest, and (ii) the initial direction of the raster scanning AFM tip upon the first encounter (i.e. positive or negative), the time taken between initial encounter of some particle at pixel position $(p_{X,Y})_{start}$ and its later possible observation at some pixel coordinate $(p_{X,Y})_{observe}$ will be defined by the return interval, Δt_{ret} , given by Eqn. 7a (for a positive/negative raster scan sequence) and Eqn. 7b (for a negative/positive raster sequence). Some additional useful extensions of the return time come from a pixel-by-pixel consideration of the minimum (Eqn. 7c) or maximum (Eqn. 7d) return time (selected from positive/negative or negative/positive scan directions). All four versions of the return time are shown schematically as a temporal map in Fig.5.

$$\Delta t_{ret(pos/neg)} \left((p_{X,Y})_{observe} \right) = t_{scan} - t_{pos} \left((p_{X,Y})_{start} \right) + t_{neg} \left((p_{X,Y})_{observe} \right) \quad (7a)$$

$$\Delta t_{ret(neg/pos)} \left((p_{X,Y})_{observe} \right) = t_{scan} - t_{neg} \left((p_{X,Y})_{start} \right) + t_{pos} \left((p_{X,Y})_{observe} \right) \quad (7b)$$

$$\Delta t_{ret(min)} \left((p_{X,Y})_{observe} \right) = \min(\Delta t_{ret(pos/neg)}, \Delta t_{ret(neg/pos)}) \quad (7c)$$

$$\Delta t_{ret(max)} \left((p_{X,Y})_{observe} \right) = \max(\Delta t_{ret(pos/neg)}, \Delta t_{ret(neg/pos)}) \quad (7d)$$

At a later time, defined by the return period Δt_{ret} , the q-type particle’s random (Brownian) motion, can be predicted using the two-dimensional diffusion probability density function, $C(\mathbf{r}, \Delta t_{ret})$, which describes the redistribution of species q to some new position $\mathbf{r}(\Delta t_{ret}) = [x_b, y_b]$ (separated by a distance $\Delta r = |\mathbf{r}(\Delta t_{ret}) - \mathbf{r}(t_0)|$) (Eqn. 8a) [61,62]. The probability of finding the particle within a particular square pixel element of area on the plane can be gotten by numerically integrating the probability density function in two dimensions (Eqn. 8b). To assist the numerical solution to approach the continuum limit each pixel was divided into approximately 100 subpixels and the pixel value evaluated via summation of the subpixel probabilities.

$$C(\mathbf{r}, t = \Delta t_{ret}) = \left(\frac{1}{4\pi D_i t} \right) e^{-\left(\frac{-\Delta r^2}{4D_i t} \right)} \quad (8a)$$

$$P \left((p_{X,Y})_{observe}, t = \Delta t_{ret} \right) \approx C(\mathbf{r}, t) \Delta x_{pixel} \Delta y_{pixel} \quad (8b)$$

In the present case the property of assignability relates to the particle’s continuing presence within the image area between successive frames of the AFM scan. Therefore, to answer the question of which situations are assignable we must evaluate the probability, $B((p_{XY})_{start}, t = \Delta t_{ret})$ (Eqn. 9) that a particle, initially located at pixel $(p_{XY})_{start}$ will still be observable within the scan area based on its diffusion coefficient, its initial position and the minimum return time corresponding to its initial position.

$$B((p_{X,Y})_{start}, t = \Delta t_{ret}) \approx \sum_{X=1}^{X=x_{max}/x_{min}} \sum_{Y=1}^{Y=y_{max}/y_{min}} P \left((p_{X,Y})_{observe}, \Delta t_{ret} \right) \quad (9)$$

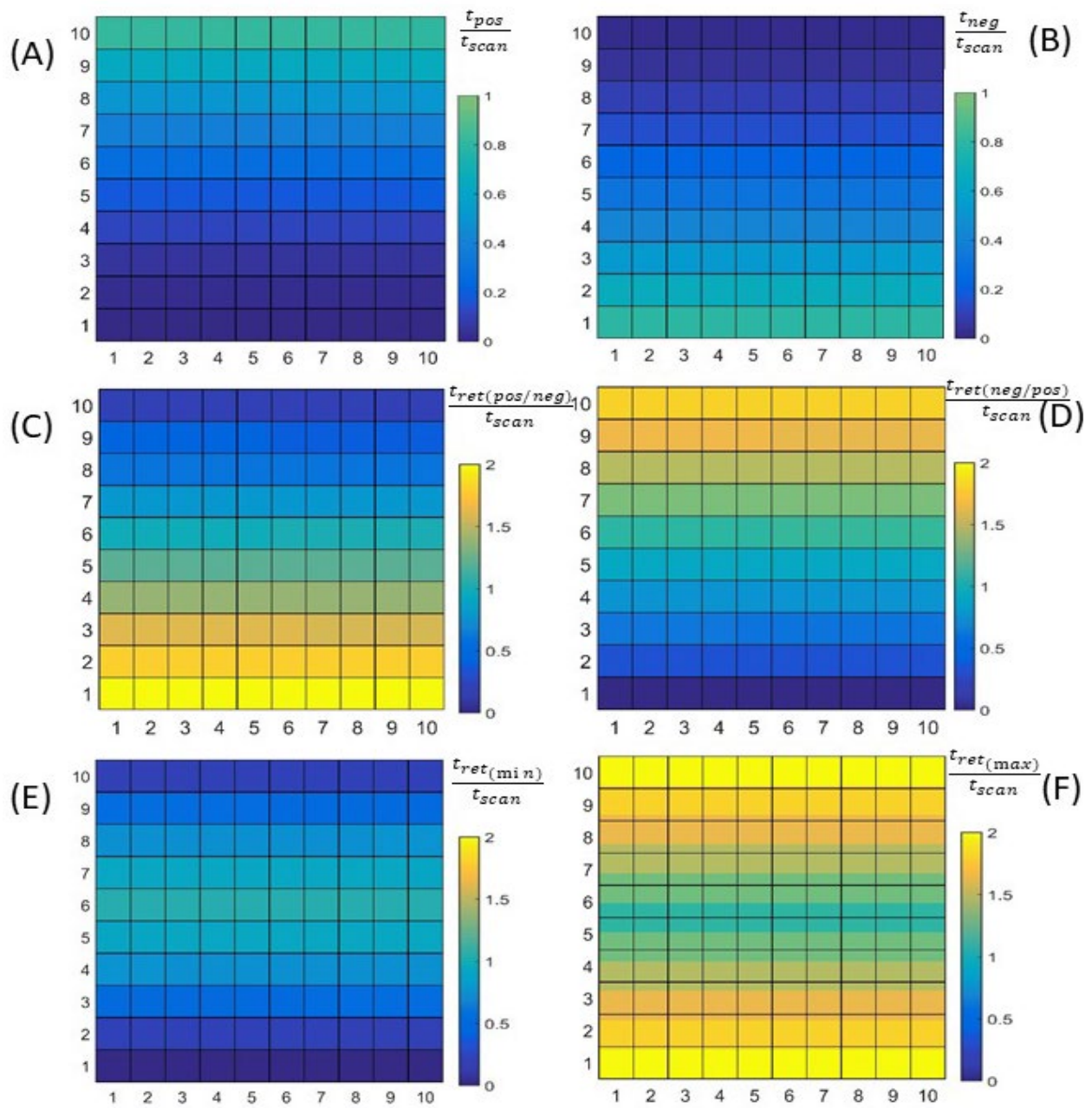


Figure 5 Useful considerations of normalized time in an AFM experiment defined according to pixel position and scan direction: Top Row – Directional scan encounter time (Eqn. 4) (A) $t_{pos}(p_{X,Y})$ - Positive scan time to arrive at position $p_{X,Y}$ starting from $p_{1,1}$, (B) $t_{neg}(p_{X,Y})$ - Negative scan time to arrive at position $p_{X,Y}$ starting from $p_{1,10}$ (normalized against t_{SCAN}). Middle Row – Return time based on time take to revisit $p_{X,Y}$ starting position i.e. $(p_{X,Y})_{observe} = (p_{X,Y})_{start}$ (Eqn. 7a,b) (C) $\Delta t_{ret(pos,neg)}(p_{X,Y})$ - Positive-negative return time and (D) $\Delta t_{ret(neg,pos)}(p_{X,Y})$ - Negative-positive return time (normalized against t_{SCAN}). Bottom Row – Minimum and maximum return times to revisit $p_{X,Y}$ starting position regardless of scan direction (Eqn. 7c,d) (E) $\Delta t_{ret(min)}(p_{X,Y})$ - Minimum value of return time and (F) $\Delta t_{ret(max)}(p_{X,Y})$ - Maximum value return time (normalized against t_{SCAN}).

Figure 6 shows a multi-panel graph showing the evaluation of the assignability, $B((p_{X,Y})_{start}, t)$ (Eqn. 6) for the three different diffusion coefficients (shown in Table 1) and three different scan times (with return times calculated for each pixel on the basis of Eqns. 7a for the positive, negative scan direction). From Fig. 6 we note that some locations afford a better opportunity for subsequent localization on the return pass than others (when the scanned image area is an open sub-

system of a greater area). This position dependence is due to both the position dependent nature of the scan return time and the position dependent propensity of the particle for moving outside the area of observation.

Having established a methodology for assessing assignability (as well as defining realistic limits for what region of the parameter spectrum we could reasonably expect to achieve feature assignment) we now proceed to outline a general method for estimating spatial assignment for any particular mobile system studied by AFM.

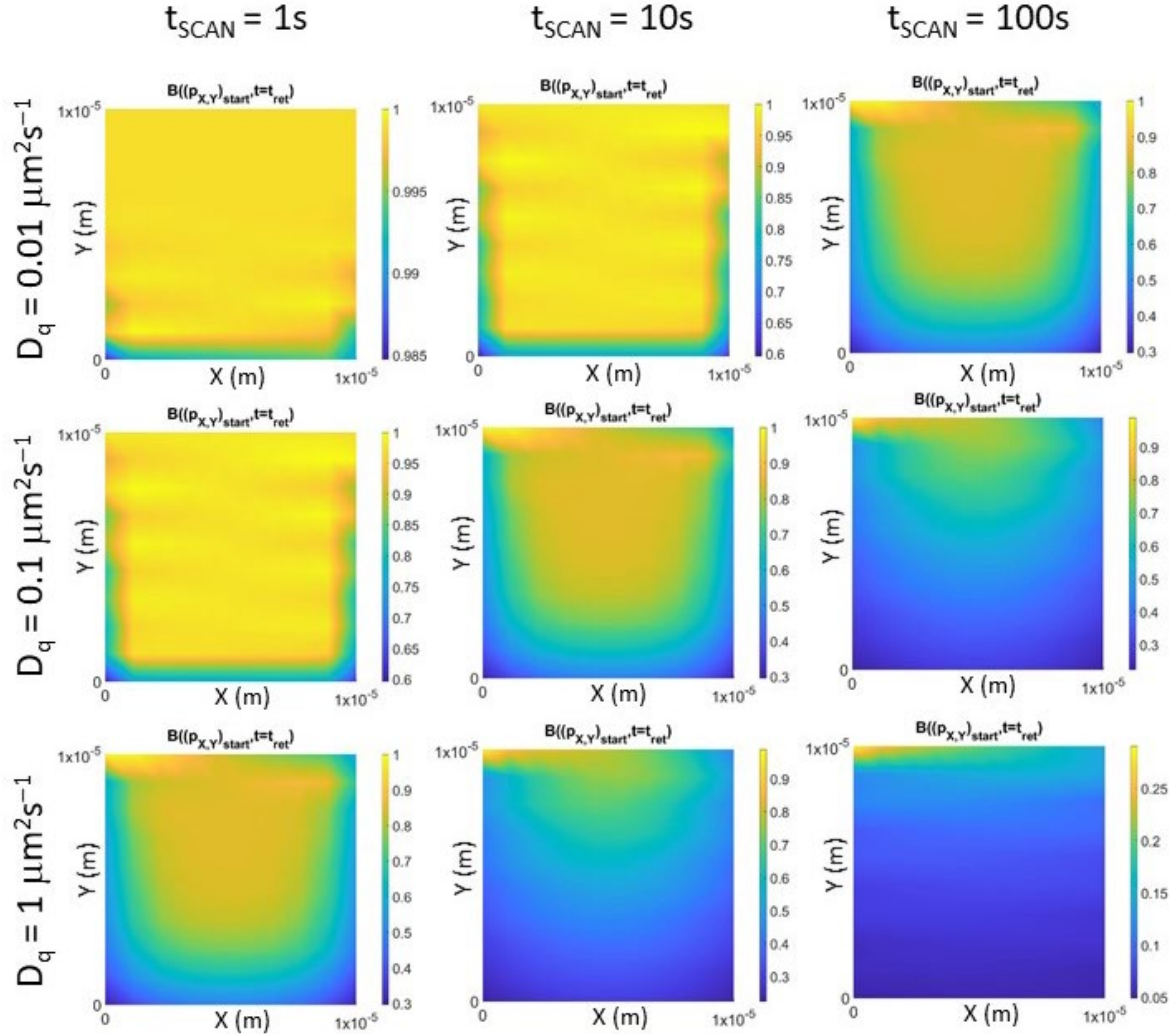


Figure 6 Evaluation of $B((\mathbf{p}_{X,Y})_{start}, t = \Delta t_{ret})$ the potential ‘assignability’ of a particle according to Eqn. 9 based on its (i) initial position $(\mathbf{p}_{X,Y})_{start}$, (ii) the size of the region of interest, (iii) return time to each observable position, $(\mathbf{p}_{X,Y})_{observe}$ (based on the positive negative scan time), and (iv) the particle’s diffusion coefficient. In these simulations the scanned area side length was set to $10 \mu\text{m}$. (Note for each figure the color bar scale describes the probability $B((\mathbf{p}_{X,Y})_{start}, t = \Delta t_{ret})$ but the color scale is not equivalent between figures. Color surfaces were generated by interpolation using values generated for a 10×10 grid).

(ii.) Spatial ‘Assignment’ for a Single Molecule

Initially we consider the situation of a single mobile q-type molecule comports to the ‘most assignable’ case described in Fig. 6 i.e. the slowest diffusion coefficient ($D_q = 0.01 \mu\text{m}^2\text{s}^{-1}$) with the fastest raster scan rate ($t_{SCAN} = 1 \text{ s}$). The mobile q-type particle is initially located at one of nine positions within a scanned area of side length $10 \mu\text{m}$ and is probed with a minimal sampling (pixel) distance $x_{min} = 100 \text{ nm}$ (Fig. 7). Due to the symmetry property associated with the raster scanning and the selected positions we consider only a single directional return time based on the positive-negative transition (Eqn. 7a) trusting the reader to perform any required transformation for other return time possibilities for other raster scanning patterns – see Supp. 2 and 3. As can be seen from Fig. 7a and b when diffusion is relatively slow in relation to the scan

rate, the average dispersion of the positional probability is limited, with this dispersion proceeding in a roughly diffusive manner i.e. the mean squared displacement (Eqn. 10a) is approximately linear with time and the average displacement in the x and y directions (Eqn. 10b and c) is very close to zero. Note that Eqns. 10a-c are all ‘renormalized’ to account for the fact that the finite area does not contain the entire probability density after a certain time.

$$\langle |\Delta \mathbf{r}|^2 \rangle_{\text{eff}}(t) = \frac{\sum_{x_{\min}}^{x_{\max}} \sum_{y_{\min}}^{y_{\max}} p((p_{X,Y})_{\text{observe},t}) |\Delta \mathbf{r}|^2 q}{\sum_{x_{\min}}^{x_{\max}} \sum_{y_{\min}}^{y_{\max}} p((p_{X,Y})_{\text{observe},t})} \quad (10a)$$

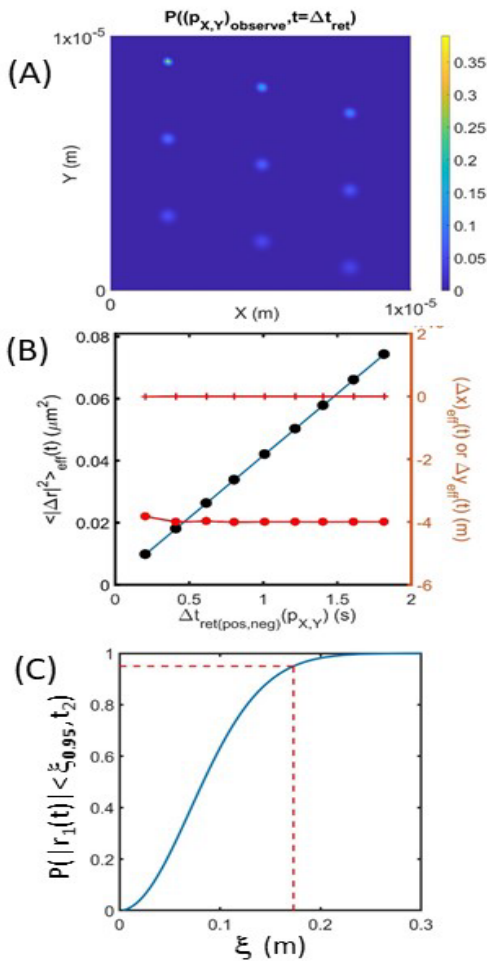
$$\langle \Delta x \rangle_{\text{eff}}(t) = \frac{\sum_{x_{\min}}^{x_{\max}} \sum_{y_{\min}}^{y_{\max}} p((p_{X,Y})_{\text{observe},t}) \Delta x}{\sum_{x_{\min}}^{x_{\max}} \sum_{y_{\min}}^{y_{\max}} p((p_{X,Y})_{\text{observe},t})} \quad (10b)$$

$$\langle \Delta y \rangle_{\text{eff}}(t) = \frac{\sum_{x_{\min}}^{x_{\max}} \sum_{y_{\min}}^{y_{\max}} p((p_{X,Y})_{\text{observe},t}) \Delta y}{\sum_{x_{\min}}^{x_{\max}} \sum_{y_{\min}}^{y_{\max}} p((p_{X,Y})_{\text{observe},t})} \quad (10c)$$

In defining spatial ‘assignment’ we seek to determine the maximum distance, ξ , that a single q-type molecule identified in one movie frame, may travel before we are unsure that it is the same molecule in the next consecutive movie frame, taken after a time interval Δt [5,65-67]. In the ‘diffusion-like’ regime we can answer the question of spatial assignment quite simply by analytically evaluating the integral form of the probability density function (Eqn. 11a) with the added condition that the degree of confidence be set to 0.95 to produce a position dependent estimate of the spatial resolution (Eqn. 11b) (Fig. 7c).

$$P(|\mathbf{r}_1(t_2)| < \xi, t_2 = \Delta t_{\text{ret}}) = \int_{\theta=0}^{\theta=2\pi} \int_{r=0}^{r=\xi} C(r, t_2) r \cdot d\theta \cdot dr = 1 - e^{-\left(\frac{\xi^2}{D_q \Delta t_{\text{ret}}(p_{X,Y})}\right)} \quad (11a)$$

$$\xi_{0.95} \approx 1.731 \sqrt{D_q \Delta t_{\text{ret}}(p_{X,Y})} \quad (11b)$$



Taking advantage of the scaling property inherent in the diffusion equation we define a composite parameter, χ_q (where $\chi_q = D_q t_{\text{SCAN}}$), to explore the effect of raster scanning on the measurement as the operative parameters depart from the diffusion-like regime (as shown in Fig. 7) with the results shown in Fig. 8 (noting that the Einstein diffusion relation in two-dimensions $\langle |\Delta \mathbf{r}|^2 \rangle = 4D_q \Delta t_{\text{ret}}$ implies that it is the product of the diffusion coefficient and the return time that determines the average squared displacement). We note that when the raster scanning is slow in relation to particle diffusion the reported behavior appears non-diffusive in the sense that the mean squared

Figure 7 Evaluation of ‘best case’ for single particle assignment ($D_q = 0.01 \mu\text{m}^2\text{s}^{-1}$) for nine initial starting positions at the fastest scanning rate $t_{\text{SCAN}} = 1$ s (with the positive, negative return time based on this scan speed used to estimate the probability for a scanned image area of $10\mu\text{m} \times 10\mu\text{m}$). (A) $P((p_{X,Y})_{\text{observe}}, t = \Delta t_{\text{ret}})$ as a function of position: Even in this best parameter case scenario (fast scan, slow diffusion) a positional dependence is seen with regard to the spatial assignment window. (B) Evaluation of diffusive character of AFM scan: At a fast scanning speed the radial spread of probability appears diffusive (i.e. mean squared displacement – blue line (Eqn. 10a) is linear with time and the average x (red +) and y (red •) displacement (Eqn. 10b and c) is close to (or effectively) zero. (C) Estimation of cumulative probability as a function of ξ : Within the apparent diffusive regime we can estimate the position of a single particle within the scanned image area with arbitrary confidence using Eqn. 11 (red dotted line indicates positional assignment with 95% confidence for the central particle shown in (A)).

displacement is not linear in χ_q and the average x and y displacements significantly deviate from zero (Fig. 8F) (off centered). Aside from these derived parameters one can directly observe that the recorded probability profile becomes distorted and highly asymmetric across the series (Fig. 8A-E). As for the previous section on the question of assignability, the estimation of ‘spatial assignment’ in such circumstances becomes somewhat complex as the recorded profile reflects both a limited set of data (i.e. some particles have left the scanned image area) and a relative velocity effect occurring between the random particle motion and the driven AFM tip. However, plots of the type shown by Fig. 8 are useful for (i) their *a priori* ability to inform on the soundness of the chosen measurement parameters for feature assignment, and (ii) their *a posteriori* capability for inferring assignment when a straightforward interpretation is not available (e.g. Fig. 8C-E). To more fully inform on the capability for spatial assignment in AFM based observation of a single particle (Eqn. 8b) we have calculated this value for the range of the composite parameter cases, χ_q , existing within the diffusive regime ($\chi_q = [0.01, 0.1] \mu\text{m}^2$) (Fig. 9).

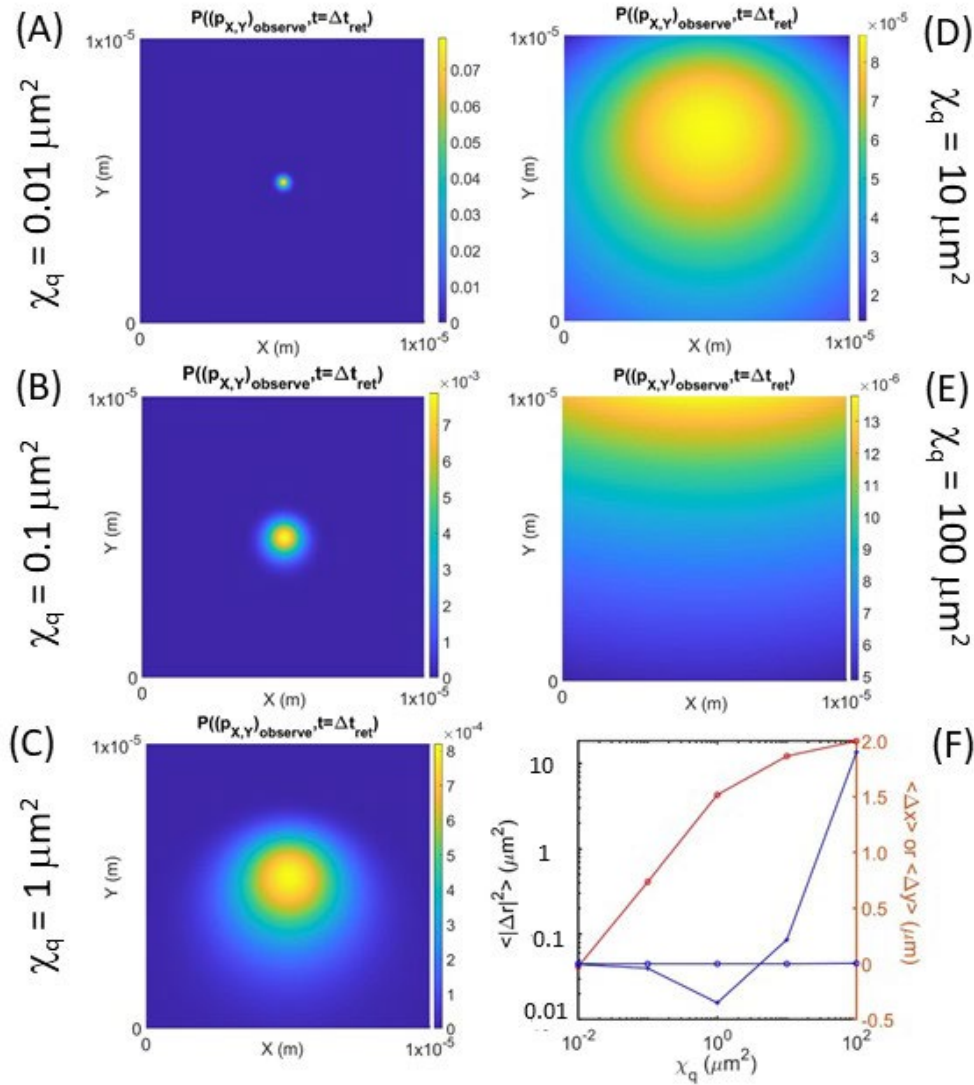


Figure 8 AFM-based probabilistic assignment of single particle motion. (A-E) AFM-based assignment of single particle motion in terms of positional encounter probability $P((p_{x,y})_{observe}, t = \Delta t_{ret})$ for a positive negative raster scanning pattern (Eqn. 8b): Composite parameter-based exposition (χ_q) of single particle assignment for the range of mobilities ($D_q = 0.01 - 1 \mu\text{m}^2\text{s}^{-1}$) and scan time ($t_{SCAN} = 1 - 100$ s) for a single central starting position $(p_{x,y})_{start}$ (located at $x = 5.0 \mu\text{m}$ and $y = 5.0 \mu\text{m}$) with the scan proceeding in the positive-negative direction for an imaged area of $10 \mu\text{m} \times 10 \mu\text{m}$. (F) Characteristic diffusive parameters: Dependence of the mean squared displacement (red •) (Eqn. 10a) and the average x (blue •) and y (blue +) displacement (Eqn. 10b and c) on the composite parameter χ_q (where $\chi_q = D_q t_{SCAN}$).

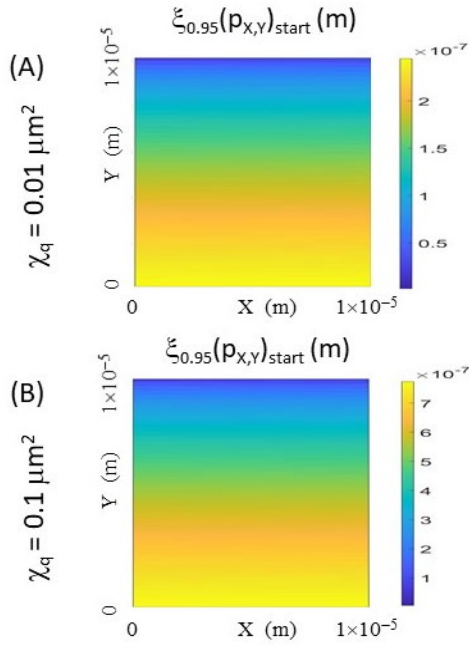


Figure 9 Evaluation of $\xi_{0.95}$ as a function of position for a single particle's diffusive motion as recorded by a positive negative raster scanning pattern. Position dependence of the assignment distance, $\xi_{0.95}$, for a single particle described at the 95% level of confidence (Eqn. 11b). The scanned image area is $10\mu\text{m} \times 10\mu\text{m}$ for the range of mobilities and scan times encompassed by the composite parameter χ_q (A) $\chi_q = 0.01 \mu\text{m}^2$ and (B) $0.1 \mu\text{m}^2$ (Evaluated for the case of the scan proceeding in the positive-negative direction - $\Delta t_{\text{ret(pos/neg)}}(\mathbf{p}_{X,Y})$ with the positional information referring to $(\mathbf{p}_{X,Y})_{\text{start}}$. Similar plots are available for other raster scanning patterns (Appendix 2 and 3).

(iii.) Spatial Assignment for the Case of Multiple Identical Molecules

Having considered the question of assignment for a single particle we now determine a practical spatial assignment limit for a q-type particle surrounded by multiple other identical q-type mobile elements, each characterized by the same measurable property (e.g. the height difference, Δz). We consider the q-type elements to be randomly distributed on the surface at an area density, ρ_q , and are therefore separated from each of their four closest nearest neighbors, on average, by a separation distance $\langle d_q \rangle = \sqrt{1/\rho_q}$ and their next four closest neighbors by a distance $\sqrt{2}\langle d_q \rangle$ (see Supp.Fig. 1). In the current work we truncate the probability evaluated in Eqn. 12c to the two nearest shells. In a similar manner to the single particle case, when defining spatial 'assignment' for a particle in a high-density arrangement, we seek to determine the maximum distance, ξ , that a single q-type molecule may travel before we are unsure that it is the same molecule in the next frame after a time interval Δt [5,67]. For the present case an equivalent way of stating this problem is to say that we wish to calculate a conditional probability, $P_{\text{res}}(\xi, \rho_q, t_2)$, where $t_2 = \Delta t_{\text{ret}}$ (Eqn. 12a), as the product of the probability that the particle of interest has not moved beyond its resolution window, $P(|\mathbf{r}_1(t_2)| < \xi, t_2)$ (Eqn. 12b). Then the probability that none of the other nearby identical mobile q-type particles (2,3,...,N) have relocated into the area coordinate set, \mathbf{A}_ξ , encompassing the circle of resolution for particle 1, will be defined by the distance ξ , i.e. $\{\prod_{j=2}^{j=N} P(\mathbf{r}_j(t_2) \notin \mathbf{A}_\xi)\}$ (Eqn. 12c).

$$P_{\text{res}}(\xi, \rho, t_2) = P(|\mathbf{r}_1(t_2)| < \xi, t_2) \left\{ \prod_{j=2}^{j=N} P(\mathbf{r}_j(t_2) \notin \mathbf{A}_\xi) \right\} \quad (12a)$$

$$P(|\mathbf{r}_1(t_2)| < \xi, t_2) = 1 - e^{-\left(\frac{\xi^2}{\sqrt{4D}t_2}\right)} \quad (12b)$$

$$\left\{ \prod_{j=2}^{j=N} P(\mathbf{r}_j(t_2) \notin \mathbf{A}_\xi) \right\} = \left\{ \prod_{j=2}^{j=N} (1 - P(\mathbf{r}_j(t_2) \in \mathbf{A}_\xi)) \right\} \quad (12c)$$

Although the evaluation of the probability shown in Eqn. 12 is simply an exercise in geometry, no analytical solution was readily achievable. In lieu of an exact result a suitable numerical approximation was used (the development of which is shown as Supplementary 1).

Figure 10 shows the spatial assignment parameter, ξ , calculated for a mobile q-type particle characterized by a particular area density, ρ_q , and diffusion coefficient, D_q . Note that a maximum exists in the probability defining the maximum spatial resolution, ξ_{max} , beyond which point the increasing possibility of substitution/confusion of the central particle for another diminishes confidence in the assignment of its identity. The existence of such a maximum represents a potentially useful way of pre-determining a minimal pixel resolution to the measurement i.e. it represents the most information that can be gotten from the AFM procedure. As this confidence maximum maps to a particular return time it will also be position dependent when conducting raster scanning. To show this we have calculated both the spatial assignment and associated confidence (probability) for each of the composite parameter cases, χ_q , within the diffusive regime (shown as Fig. 11).

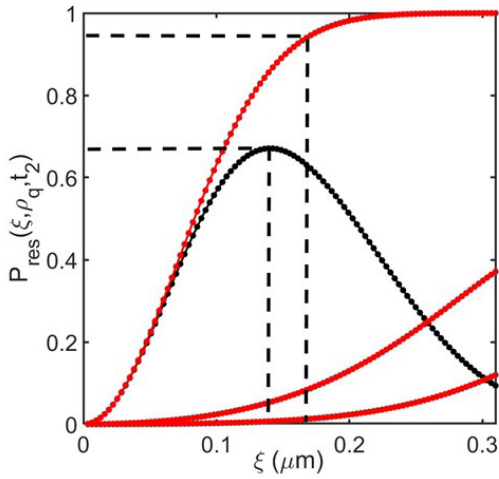


Figure 10 Evaluation of the component probabilities shown in Eqn. 12 relating to the spatial assignment of a particle surrounded by multiple copies of itself: Particle located at the central pixel (51,51) of a scanned image area containing multiple identical particles (side length $10\ \mu\text{m}$; $\rho_q = 10\ \text{particles}/\mu\text{m}^2$; $D_q = 0.01\ \mu\text{m}^2\ \text{s}^{-1}$; $t_{\text{SCAN}} = 1\ \text{s}$). The three red lines describe the component probabilities shown in Eqn. 12a for particles existing within a ($P(|r_1(t_2)| < \xi, t_2)$) radial shell of magnitude ξ (explicitly denoting particle 1, the particle of interest, and $P(r_j(t_2) \in A_\xi)$ for particles 2 to 5, (the inner shell) and $P(r_j(t_2) \in A_\xi)$ for particles 6 to 9 (the immediate outer shell) (Eqn. 12c). The solid black line describes the resultant probability $P_{res}(\xi, \rho, t_2)$. Note the black dotted lines denote both the specific value of ξ associated with the maximum confidence in positional assignment and the value of $\xi_{0.95}$ defining the radial shell defining the majority of spatial probability associated with particle 1 (Eqn. 12b).

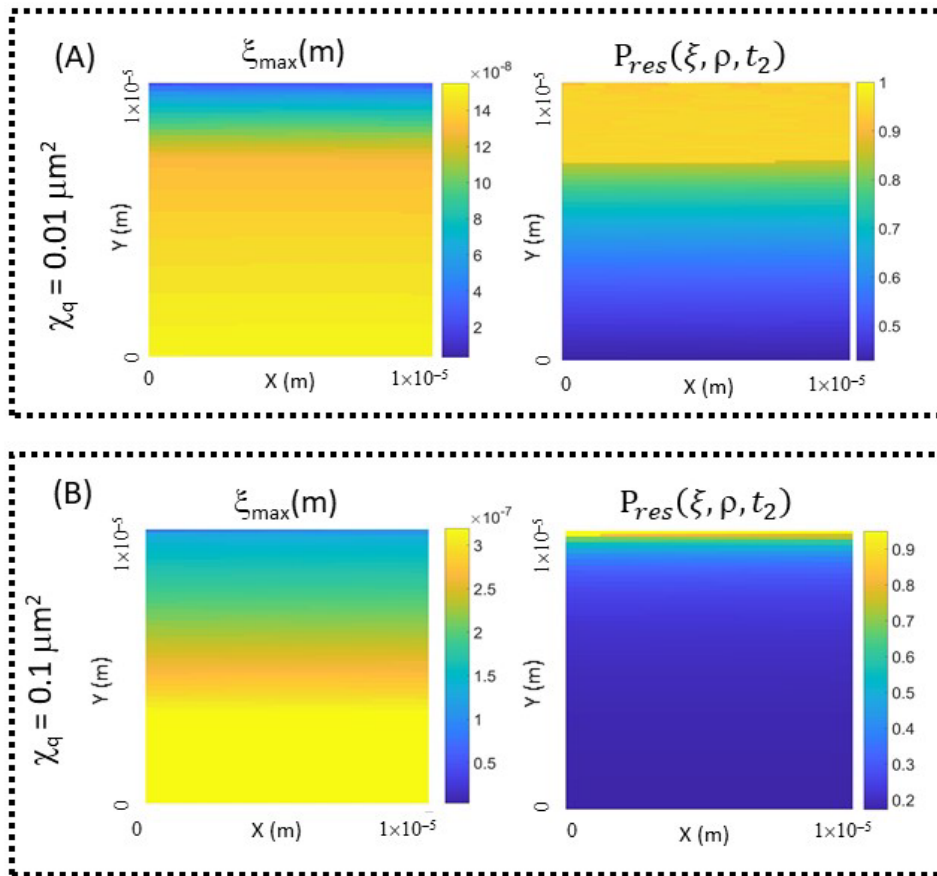


Figure 11 Position dependence of the maximal confidence associated with the assignment of a particle (initially located at $(\mathbf{p}_{X,Y})_{start}$) amongst randomly distributed replicas (multiple particle resolution) for the range of mobilities and scan times encompassed by the composite parameter χ_q (Panel (A) $\chi_q = 0.01\ \mu\text{m}^2$; Panel (B) $\chi_q = 0.1\ \mu\text{m}^2$) (with the scan proceeding in the positive-negative direction - $\Delta \mathbf{t}_{ret(pos/neg)}(\mathbf{p}_{X,Y})$ for $\rho_q = 10\ \text{particles}/\mu\text{m}^2$ in a scanned image area of $10\ \mu\text{m} \times 10\ \mu\text{m}$). (Left hand column) Position dependent resolution associated with (Right hand column) position dependent maximum level of confidence in assignment ($P_{res}(\xi, \rho, t_2)$). (Note if $\xi_{0.95} < \xi_{(P_{res})_{max}}$ then $\xi_{0.95}$ was selected). (Parameters described in Eqn. 12 and Fig. 10)

Discussion

Since its invention and application to the measurement of biological samples [14,68] AFM has greatly added to the armamentarium of cell biologists, providing them with a window into molecular level events occurring on, and within, the cell [31,69]. Later developments to increase the speed and resolution of AFM imaging [16,36,64] have made possible the observation of dynamic biological events [e.g. see 29,33,36,40,43,45,70,71]. The current work started with a general question, ‘how confidently can one relate changes observed in consecutive HS-AFM images of a living cell membrane’. To determine an answer, we approached the problem from the simplifying limit of no gross morphological change occurring in the cell structure or position (*the regime 2 to regime 3 transition described in this paper*). Within this limit, changes in membrane properties, such as local elasticity or topography, result partly (or in whole) from the intrinsic fluidity and heterogeneity of the cell membrane itself [30,38,72,73]. Through a combination of analytical and numerical descriptions of membrane diffusion, raster scanning and image pixilation we have developed systematic methodologies for answering the following three, more specific, questions,

- (i) What situations are assignable by AFM?
- (ii) How would one confidently assign the identity of a single particle in HS-AFM?
- (iii) How does the estimation of spatial assignment change when multiple copies of the particle are present?

With regards to the first question, ‘*What situations are assignable by AFM?*’, in this work we developed a process (Eqns. 4-9) for estimating the retention of a once encountered molecule within a demarcated region of measurement that exists as an open system within a larger membrane area [30,31,43]. By factoring in the AFM tip scan rate and likely component mobility values, an ‘assignability’ position dependence was determined specifically for the positive-negative return time (Fig. 6), although it is a trivial matter to apply it to any of the other versions of the return time shown in Eqn. 7 as well as for other raster scanning patterns (see Supp. 2 and 3). The simulation process also provided some quantitative backbone to the intuitive understanding that molecules identified towards the edge of the open system have intrinsically lower value in terms of meaningful assignment. Such a systematic approach to the consideration of image ‘assignability’ properties should prove useful to both experimental design and confidence assignment in post-acquisition interpretation of observed structures/properties from different areas of the obtained image [74,75].

To provide an answer to the second question, ‘*How would one confidently assign the identity of a single particle in HS-AFM?*’, we first developed processes to both, simulate the non-instantaneous AFM-based measurement of a single-particle undergoing random Brownian movement, and identify when the AFM measurement process would report the intrinsically diffusive behavior as not being so (Eqns. 10). When system parameters lie within this characteristic diffusion limit, the integrated form of the diffusion equation may be used to *a priori* determine a spatial assignment value, ξ , to an arbitrary level of confidence (Eqn. 11). In the present work we used 95% due to its well understood association with normal statistical tables of approximately 2 standard deviations [76]. The practical meaning of $\xi_{0.95}$ in Eqn. 11 is that it defines the circular area on the membrane, centered around the point of first contact, within which the particle will likely exist at the time of the next AFM measurement. This process could be potentially useful in the design of experiments aimed at analyzing the behavior of distinctive single particles existing within the scanned image (such as for the case of labelled lipids or proteins or relatively rare (in the observation sense) labeled integral membrane proteins, complexes or separate microphases [77]) in two different ways. When high-resolution single particle tracking is the object of study, such information could be used to *a priori* define the upper limiting value of the image pixilation density and hence the pixel size (i.e. Δx_{pixel} , Δy_{pixel}) beyond which potentially important spatial information would be lost. Alternatively, $\xi_{0.95}$, could be used to inform on minimum pixel spacing when optimizing the high-speed recording of gross cell morphology using a low-resolution, large diameter AFM tip in intermittent raster scanning mode. It is important to realize that the developed formalism [Eqns. 7-10] does not lose its value when the relationship between AFM instrument parameters and the intrinsic membrane dynamics lie beyond the diffusion regime identified by Eqn. 6 and 7. They can still be used to inform on most probable assignment (e.g. Fig. 8C-E) however the problem now loses its circular symmetry and requires that the predicted probability profile be used directly (rather than in the simplified form described in Eqn. 11).

To generate a solution to the third question, ‘*How does the estimation of spatial assignment change when multiple copies of the particle are present?*’, we modified the single particle assignment calculation (Eqn. 11b) to factor in the conditional probability that a nearby identical particle might wander into the resolution window thereby diminishing our confidence in the assignment (Eqn. 12). This potential for substitution results in a reduced spatial resolution maximum at a lower confidence value (Figs. 10 and 11). In reality, such multiparticle situations are the most likely to be encountered experimentally, due to the fact that the tendency is always for overproduction (either when chemically labeling lipids or proteins or overexpression of genetic constructs) to facilitate easier observation [78,79]. Such density dependent effects on the assessment of required experimental parameters necessary for achieving spatial assignment could be used to inform upon optimal pixilation when the goal is to understand the growth of complexes via self-association of individual protein

subunits or alternatively the agglomeration of membrane proteins or lipids into phase separated regions [77,80]. Again, we stress that the general approach (Eqn. 12) is not compromised when experimental dictats mean that the situation is no longer ‘diffusive’ as defined by Eqn. 10 and 12. However, in such cases the problem again loses its symmetry required for simplification and would require evaluation ‘on the fly’ in terms of the asymmetric probability distribution.

Questions Related to Pixilation Choice for Dynamic Membranes

At the beginning of each HS-AFM experiment the user must make a decision upon image pixilation. By formulating the pixilation question in the fashion described in Eqn. 1, this study has teased out some points relating to the differences between static and dynamic surfaces that we now discuss. As noted in the introduction, the joint condition of fastest scan rate and largest pixel size (lowest pixel density) in the continuous sampling limit is set by the oscillation frequency, f , and diameter, ϕ , of the AFM tip, and occurs when $x_{\text{pixel}} = x_{\text{min}} = \phi$. However, two reasons may prompt an experimenter to set a pixel size that is larger than the minimum lateral and vertical sampling distances ($x_{\text{pixel}} > x_{\text{min}}$; $y_{\text{pixel}} > y_{\text{min}}$) (discussed in the introduction with reference to Figs. 1-3 and Eqn. 1). The first reason involves increasing the signal to noise ratio through oversampling, the second involves decreasing the image file size by combining multiple independent pixels into a larger pixel [21,22,31,49,64]. We note that due to the asymmetric nature of the temporal delay associated with the raster scan process in the vertical and horizontal directions (Eqn.7) any closely positioned sub-pixel pair of measured values in the same lateral scan line, $z(x_1, y_1, t_1)$ and $z(x_2, y_1, t_2)$, will tend to exhibit both a high degree of spatial and temporal correlation for both dynamic and static surfaces. However, similarly closely positioned points in the vertical scan direction, $z(x_1, y_1, t_1)$ and $z(x_1, y_2, t_n)$, will show high spatial and temporal correlation only for static surfaces. Indeed, for dynamic surfaces, any significant redistribution of surface components over the greater time interval associated with completing the vertical component of the raster scanning will diminish the spatial and temporal correlation of the measured variable. Such an understanding implies that rectangular pixilation (with the long axis of the pixel aligned with the lateral direction) may be the preferred choice as a means for achieving both enhanced signal to noise ratios and decreasing image size for dynamic surfaces. Such raster-based spatiotemporal considerations of both pixel construction and pixel-association may also prove important in the execution of the recently posited sub-pixel expansion approach [75] to dynamic surfaces, suggesting at minimum, that different weighting be applied to the interpolations made using x and y-axis components.

Assumptions on Which This Study Rests

Many types of error exist within AFM experiments [16,18]. At the device level errors due to laser intensity fluctuations, quadrant detector Shot noise, cantilever thermal Brownian noise and xyz- piezoelectric creep will all lead to positional error, however these forms of noise are not expected to be significantly time and position dependent and we have neglected their inclusion in the present work. In this study we have placed our focus on positional changes introduced by mobile elements within the membrane [38,51-55]. To develop sufficient traction to move forward we had to make a number of assumptions which, for the sake of clarity we emphasize now. The first, and perhaps most crucial assumption, was that movement within the cell membrane is solely due to its fluid nature and not the result of gross morphological change within the cell. Towards this point, the movement is a general property of all living organisms and cells grown in culture undergo movement at a number of levels [31,81,82]. Cell motion may be due to whole cell walking type processes in which the actin driven lamellipodia project from the anterior membrane to form surface adhesive junctions which can then be used to pull the cell forward [83]. Another type of gross cell movement can be affected by generalized swelling or shrinkage [84]. Examples of more localized forms of movement are those associated with membrane remodeling (endo- or exocytosis) [43,82] or cell division [41]. Nevertheless, a static cell ‘resting state’, in which large scale movements in set sub-regions or by the entire cell, either do not occur or can be rendered negligible through operation of the AFM over a much faster time scale (Regime 2 \rightarrow 3), is a known phenomenon for most cell-types, so when observation of cell movement is not the goal of the study, appropriate experimental preparation can minimize the potential complicating effects of movement during the timescale of an AFM measurement [85].

Another major assumption is that the AFM tip does not preferentially interact with mobile particles to influence their trajectory. Such behavior has been noted in the AFM-based measurement of surface defects and ad-atom motion [86,87] as well as in lateral ‘pulling’ experiments of cell membrane receptors by functionalized tips [88,89]. In general, unless interaction between the tip and the mobile surface molecule is a desired aspect of the study any such direct affinity can be eliminated (or at least minimized) by appropriate passivation of the AFM tip and use of appropriate sampling routines - such as the zero-force mode topographical measurement strategies [90]. However, in solution, interactions can also be mediated indirectly as hydrodynamic forces stemming from directed motion of the AFM tip [91]. Such motion can impart kinetic energy to the surrounding solvent, which in turn influences nearby surface molecules [61,92]. The role of such hydrodynamic mediated forces in AFM experimentation has been theoretically studied [91] and may be important if tip motion were to induce non-random behavior in the distributed surface components. If shown to be important, then two of the starting assumptions adopted in this study (diffusive motion of the membrane components and no local deformation of the cell membrane) would need to be modified.

A third major assumption is that the image area is an open system contained within a much larger equivalent membrane environment. Typical eukaryotic cells have diameters in the region of $\sim 20 \mu\text{m}$ [93] and so this assumption is not unreasonable for many cell-types, however the aspect ratio of some cell types (long and thin fibroblasts or neurons) and the reduced size of others (many prokaryotic cells have diameters 1-5 μm [93]) mean that this boundary condition will not always be the most appropriate selection.

A further assumption relates to the appropriateness of our bounding of parameter space for HS-AFM based interrogation of living cells. Within the development of our argument, we provided experimental and theoretical justification for the selected range of diffusion constants (Table 1). However, we did not fully discuss the reasoning behind our choice of ranges for AFM tip scanning rates, scanned image size and raster patterns. With regard to AFM tip scanning rates, our fastest line scanning rate of 10,000 $\mu\text{m s}^{-1}$ is representative of values currently achievable using specialist HS-AFM laboratory devices [16,36,43] whilst our slowest line scanning rate of 10 $\mu\text{m s}^{-1}$ is on par with the vast majority of commercially available AFM devices.

The question of providing spatial bounds for the scanned image is a little more complicated. Potentially, even relatively slow line-scanning rate instruments could be presented as HS-AFM devices if a suitably small image area was chosen (producing sub-second t_{SCAN} frame rates). However, when analyzing cell membrane properties the focus is to measure the cell-scale spatial distribution in the particular property of interest, making sub-micrometer distance scales problematic [28,36]. There are many examples within the AFM live cell membrane literature of AFM image areas with 10 to 40 μm side-lengths observed at frame scan times of several to tens of minutes. We have taken the point of view to use scan times ranging from 1 to 100 seconds to both inform upon results in the published literature as well as forecast what we may expect from next generation devices capable of achieving large area sub-second scan times [36,49].

The final parameter justification relates to our selection of a raster scanning pattern. Different AFM-amenable scanning profiles based on varying sinusoidal patterns, ellipses and decreasing spirals have all been suggested as potentially being superior to the standard back and forth raster pattern described here [24,25] (although we note that these assessments have been solely made in regard to the imaging of static unchanging surfaces). However, the standard raster pattern is a commonly adopted pattern in commercial instrumentation and thus our choice is representative of much published literature [17,49,69]. A related raster scan profile that is used in some laboratory-built AFM devices is the revolving back and forth raster pattern in which, after completion of one positive scan profile, the tip is translated back to the beginning of the image frame [36]. Another type of related scan profile is the uniformly same direction pattern recently introduced by Fukuda and Ando [9] in which both the line and vertical scanning both occur in the same direction throughout the scan. This latter approach has been shown to have the added benefits of simplifying feedback control of the HS-AFM tip and also greatly maintain sample integrity in biological HS-AFM experiments. Both the revolving and uniform direction raster profiles offer potential benefits in producing a regular return time for each pixel independent of its position within the imaged area. However, on the down side, the lack of a reverse scan capability potentially limits the advantages described in Fig. 4 E and F that are associated with the ability to analyze positional information associated with minimum (faster) and maximum (slower) return times. Importantly neither completely mitigate the potential for directional scan bias influencing the symmetry of the assignment envelope (for example see Supplementary 2).

How Our Work Differs from Previous Studies

Although the problem discussed here (AFM measurements of dynamic surfaces) is important for inferring meaning from AFM-based cell biology experiments, there has been surprisingly little work done to address it. Earlier studies by the groups of Greve and Scheuring [6,7] treated a similar problem that related to machine drift between AFM scans but paid less attention to sample component motion within the scan (beyond describing the motion as diffusive). More recently Kubo et al. have applied a Bayesian-based post-processing technique for recreation of more accurate estimates of highly dynamic large biological structures that span multiple pixels within the image [8]. Although the techniques described in that paper refer to specifically to structure estimation, the Bayesian approach described by Kubo et al. [8] could be adapted to the case of feature assignment in both the diffusive (Figs 7A,B) and non-diffusive regimes (Figs 7C-E). However, the major point of this paper is in establishing optimal conditions, prior to experiment, that will maximize data quality and afford easiest interpretability. In terms of the type of problem addressed (i.e. interpretation of dynamic biological surface) this work differs substantially from recent efforts that have concentrated on attaining super high-resolution information from static biological images acquired by HS-AFM methodology e.g. [75]. As the HS-AFM technique improves (becoming faster and less perturbing) the relationship between the relative dynamics of instrument/measurement and biology will change. During this technological evolution it is our belief that the dynamic considerations espoused within the current work will become increasingly important.

Checklist for Experimentalists

At a very practical level this paper has presented simple formalism (easily realizable via spread sheet evaluation) that is both able to provide an estimate of biologically relevant quantities and use the basic parameters of an AFM experiment

(e.g. line scanning speed, minimal xy-sampling dimensions, minimum pixilation dimensions and scanned image size) to deduce more useful complex composite instrument terms. These biological and machine related quantities include,

- (i) Pixel dependent scan arrival time (Eqn. 4)
- (ii) Membrane component motion (Eqn. 6, 7)
- (iii) Pixel dependent scan return time (Eqn. 7)
- (iv) Positional image confidence (Eqn. 8 and 9)
- (iv) Characteristic diffusive regime (Eqn. 10 and 11)

A slightly more difficult implementation of the information included in this paper relates to the specification of density dependent assignment confidence intervals (Eqn. 12, Fig. 11) (but the procedures for its numerical implementation outlined within Supplementary 1 should not be beyond most scientists). To provide some assistance we have developed a standalone application called HS-AFM UGOKU (HS-AFM Users' Graphical Optimization tool from Kanazawa University) (Supplementary 3). Available upon request from the authors via email and also available for download at the authors' institutional websites, the HS-AFM UGOKU application takes the scanned image dimensions, the tip diameter and tip oscillation frequency, the dynamic particles dimensions, diffusion constant and surface density and outputs the position and density dependent data described within this paper. Users can employ this tool to pre-optimize their experiment in an iterative graphical fashion. Some screenshots and a basic description of the procedure for usage of the HS-AFM UGOKU software is given as supplementary data to this paper (Supplementary 3).

Concluding Remarks

What started off as a simple quest for understanding how confident one can be in assigning changes observed between movie frames of HS-AFM live cell imaging has potentially resulted in the development of a new method for optimizing AFM design in terms of the selection of the most parsimonious combination of image size, the AFM tip properties, scanning rate and the degree of pixilation within the measured area. With regards to this last point we note the rather interesting results of Eqn. 12 (shown in Fig. 11 and 12) which suggests an optimal pixel spacing facilitating assignment confidence that is cognizant of component density (and not just its intrinsic mobility).

Although the current work has emphasized topography as the measurement variable, it should be recognized that the arguments are general and just as applicable to other commonly measured properties of the fluid-membrane bilayer such as local elasticity [30,94], local binding affinity [69,88] and /or the position-dependent penetration force [95,96]. In conceptualizing such cases we may think of the mobile component as a composite of lipids and proteins able to be assigned a phenomenological diffusion coefficient of arbitrary size and mobility.

We hope that the theoretical considerations developed here may prove useful to scientists using AFM in both the design and interpretation of their experiments. It is also hoped that the present work may stimulate further investigations into the limits of the HS-AFM based measurement of dynamic biological surfaces and promote a greater understanding of interfacial biophysics [97] in general.

Conflict of Interest

D.H. reports no conflict of interest. A.S.F. reports no conflict of interest. No humans or animals were harmed in the writing of this manuscript.

Author Contributions

The concepts in this paper were developed together by the two authors. D.H. wrote the first draft. A.S.F and D.H. produced the final draft together.

Acknowledgements

We appreciate comments made (on a previous draft) from Filippo Federici Canova, Ondrej Krejci, Holger Flechsig, Takashi Sumikama, Ayhan Yurtsever, Clemens Franz and Takeshi Fukuma. We would also like to acknowledge the anonymous Reviewers of this manuscript for useful queries and suggestions. DH acknowledges funding associated with the receipt of a Tokunin Assistant Professorship carried out at the WPI-Center for Nano Life Science, Kanazawa University. DH also acknowledges the University of Aalto, for an appointment to their Affiliated Researcher Program carried out within the Department of Applied Physics. This work supported, in part, by KAKENHI Start-Up grant 21K20633 awarded to D.H. and the Academy of Finland under Project No. 314862 awarded to A.S.F.

References

- [1] Kusumi, A., Nakada, C., Ritchie, K., Murase, K., Suzuki, K., Murakoshi, H., et al. Paradigm shift of the plasma membrane concept from the two-dimensional continuum fluid to the partitioned fluid: High-speed single-molecule tracking of membrane molecules. *Annu. Rev. Biophys. Biomol. Struct.* 34, 351-378 (2005). <https://doi.org/10.1146/annurev.biophys.34.040204.144637>
- [2] Saxton, M. J. Single-particle tracking: Connecting the dots. *Nat. Methods* 5, 671-672 (2008). <https://doi.org/10.1038/nmeth0808-671>
- [3] Shen, H., Tazuin, L. J., Baiyasi, R., Wang, W., Moringo, N., Shuang, B., et al. Single particle tracking: From theory to biophysical applications. *Chem. Rev.* 117, 7331-7376 (2017). <https://doi.org/10.1021/acs.chemrev.6b00815>
- [4] Tinevez, J. Y., Perry, N., Schindelin, J., Hoopes, G. M., Reynolds, G. D., Laplantine, E., et al. TrackMate: An open and extensible platform for single-particle tracking. *Methods* 115, 80-90 (2017). <https://doi.org/10.1016/j.ymeth.2016.09.016>
- [5] Teraguchi, S., Kumagai, Y. Estimation of diffusion constants from single molecular measurement without explicit tracking. *BMC Syst. Biol.* 12, 25-39 (2018). <https://doi.org/10.1186/s12918-018-0526-5>
- [6] Van Noort, S. J. T., van der Werf, K. O., de Grooth, B. G., Greve, J. High speed atomic force microscopy of biomolecules. *Biophys. J.* 77, 2295-2303 (1999). [https://doi.org/10.1016/S0006-3495\(99\)77068-2](https://doi.org/10.1016/S0006-3495(99)77068-2)
- [7] Husain, M., Boudier, T., Paul-Gilloteaux, P., Casuso, I., Scheuring, S. Software for drift compensation, particle tracking and particle analysis of high-speed atomic force microscopy image series. *J. Mol. Recognit.* 25, 292-298 (2012). <https://doi.org/10.1002/jmr.2187>
- [8] Kubo, S., Kato, S., Nakamura, K., Kodera, N., Takada, S. Resolving the data asynchronicity in high-speed atomic force microscopy measurement via the Kalman Smoother. *Sci. Rep.* 10, 18393 (2020). <https://doi.org/10.1038/s41598-020-75463-1>
- [9] Fukuda, S., Ando, T. Faster high-speed atomic force microscopy for imaging of biomolecular processes. *Rev. Sci. Instrum.* 92, 033705 (2021). <https://doi.org/10.1063/5.0032948>
- [10] Shibata, M., Watanabe, H., Uchihashi, T., Ando, T., Yasuda, R. High-speed atomic force microscopy imaging of live mammalian cells. *Biophys. Physicobiol.* 14, 127-135 (2017). https://doi.org/10.2142/biophysico.14.0_127
- [11] Casuso, I., Khao, J., Chami, M., Paul-Gilloteaux, P., Husain, M., Duneau, J. P., et al. Characterization of the motion of membrane proteins using high-speed atomic force microscopy. *Nat. Nanotechnol.* 7, 525-529 (2012). <https://doi.org/10.1038/nnano.2012.109>
- [12] Viani, M. B., Schäffer, T. E., Paloczi, G. T., Pietrasanta, L. I., Smith, B. L., Thompson, J. B., et al. Fast imaging and fast force spectroscopy of single biopolymers with a new atomic force microscope designed for small cantilevers. *Rev. Sci. Instrum.* 70, 4300-4303 (1999). <https://doi.org/10.1063/1.1150069>
- [13] Ando, T., Kodera, N., Takai, E., Maruyama, D., Saito, K., Toda, A. A high-speed atomic force microscope for studying biological macromolecules. *Proc. Natl. Acad. Sci. U.S.A.* 98, 12468-12472 (2001). <https://doi.org/10.1073/pnas.211400898>
- [14] Binnig, G., Quate, C. F., Gerber, C. Atomic force microscope. *Phys. Rev. Lett.* 56, 930-933 (1986). <https://doi.org/10.1103/PhysRevLett.56.930>
- [15] Alessandrini, A., Facci, P. AFM: A versatile tool in biophysics. *Meas. Sci. Technol.* 16, R65 (2005). <https://doi.org/10.1088/0957-0233/16/6/R01>
- [16] Ando, T., Uchihashi, T., Fukuma, T. High-speed atomic force microscopy for nano-visualization of dynamic biomolecular processes. *Prog. Surf. Sci.* 83, 337-437 (2008). <https://doi.org/10.1016/j.progsurf.2008.09.001>
- [17] Eaton, P., West, P. *Atomic force microscopy* (Oxford University Press, UK, 2010).
- [18] Garcia, R., Perez, R. Dynamic atomic force microscopy methods. *Surf. Sci. Rep.* 47, 197-301 (2002). [https://doi.org/10.1016/S0167-5729\(02\)00077-8](https://doi.org/10.1016/S0167-5729(02)00077-8)
- [19] Mendez-Vilas, A., Bruque, J. M., González-Martín, M. L. Sensitivity of surface roughness parameters to changes in the density of scanning points in multi-scale AFM studies. Application to a biomaterial surface. *Ultramicroscopy* 107, 617-625 (2007). <https://doi.org/10.1016/j.ultramic.2006.12.002>
- [20] Ando, T., Kodera, N., Maruyama, D., Takai, E., Saito, K., Toda, A. A high-speed atomic force microscope for studying biological macromolecules in action. *Jpn. J. Appl. Phys.* 41, 4851 (2002). <https://doi.org/10.1143/JJAP.41.4851>
- [21] Burger, W., Burge, M. J. *Principles of digital image processing*, Vol. 54 (Springer, London, 2009).
- [22] Rana, M. S., Pota, H. R., Petersen, I. R. Improvement in the imaging performance of atomic force microscopy: A survey. *IEEE Trans. Autom. Sci. Eng.* 14, 1265-1285 (2016). <https://doi.org/10.1109/TASE.2016.2538319>
- [23] Payton, O. D., Picco, L., Miles, M. J., Homer, M. E., Champneys, A. R. Improving the signal-to-noise ratio of high-speed contact mode atomic force microscopy. *Rev. Sci. Instrum.* 83, 083710 (2012). <https://doi.org/10.1063/1.4747455>
- [24] Teo, Y. R., Yong, Y., Fleming, A. J. A comparison of scanning methods and the vertical control implications for

- scanning probe microscopy. *Asian J. Control* 20, 1352-1366 (2018). <https://doi.org/10.1002/asjc.1422>
- [25] Rana, M. S., Pota, H. R., Petersen, I. R. Development of scanning methods in AFM imaging. in *Proc. Int. Conf. Elect. Electron. Ind. Automat.*, pp. 97-106.
- [26] Das, S. K., Badal, F. R., Rahman, M. A., Islam, M. A., Sarker, S. K., Paul, N. Improvement of alternative non-raster scanning methods for high-speed atomic force microscopy: A review. *IEEE Access* 7, 115603-115624 (2019). <https://doi.org/10.1109/ACCESS.2019.2936471>
- [27] Häberle, W., Höber, J. K. H., Ohnesorge, F., Smith, D. P. E., Binnig, G. In situ investigations of single living cells infected by viruses. *Ultramicroscopy* 42-44, 1161-1167 (1992). [https://doi.org/10.1016/0304-3991\(92\)90418-j](https://doi.org/10.1016/0304-3991(92)90418-j)
- [28] Radmacher, M., Tillmann, R. W., Fritz, M., Gaub, H. E. From molecules to cells: Imaging soft samples with the atomic force microscope. *Science* 257, 1900-1905 (1992). <https://doi.org/10.1126/science.1411505>
- [29] Yamashita, H., Taoka, A., Uchihashi, T., Asano, T., Ando, T., Fukumori, Y. Single-molecule imaging on living bacterial cell surface by high-speed AFM. *J. Mol. Biol.* 422, 300-309 (2012). <https://doi.org/10.1016/j.jmb.2012.05.018>
- [30] Roduit, C., Van Der Goot, F. G., De Los Rios, P., Yersin, A., Steiner, P., Dietler, G., et al. Elastic membrane heterogeneity of living cells revealed by stiff nanoscale membrane domains. *Biophys. J.* 94, 1521-1532 (2008). <https://doi.org/10.1529/biophysj.107.112862>
- [31] Kodera, N., Ando, T. Visualization of intrinsically disordered proteins by high-speed atomic force microscopy. *Curr. Opin. Struct. Biol.* 72, 260-266 (2022). <https://doi.org/10.1016/j.sbi.2021.11.014>
- [32] Shan, Y., Wang, H. The structure and function of cell membranes examined by atomic force microscopy and single-molecule force spectroscopy. *Chem. Soc. Rev.* 44, 3617-3638 (2015). <https://doi.org/10.1039/C4CS00508B>
- [33] Seifert, J., Rheinlaender, J., Novak, P., Korchev, Y. E., Schäffer, T. E. Comparison of atomic force microscopy and scanning ion conductance microscopy for live cell imaging. *Langmuir* 31, 6807-6813 (2015). <https://doi.org/10.1021/acs.langmuir.5b01124>
- [34] Baaden, M. Visualizing biological membrane organization and dynamics. *J. Mol. Biol.* 431, 1889-1919 (2019). <https://doi.org/10.1016/j.jmb.2019.02.018>
- [35] Zeno, W. F., Day, K. J., Gordon, V. D., Stachowiak, J. C. Principles and applications of biological membrane organization. *Annu. Rev. Biophys.* 49, 19-39 (2020). <https://doi.org/10.1146/annurev-biophys-121219-081637>
- [36] Marchesi, A., Umeda, K., Komekawa, T., Matsubara, T., Flechsig, H., Ando, T. An ultra-wide scanner for large-area high-speed atomic force microscopy with megapixel resolution. *Sci. Rep.* 11, 13003 (2021). <https://doi.org/10.1038/s41598-021-92365-y>
- [37] Fantner, G. E., Barbero, R. J., Gray, D. S., Belcher, A. M. Kinetics of antimicrobial peptide activity measured on individual bacterial cells using high-speed atomic force microscopy. *Nat. Nanotechnol.* 5, 280-285 (2010). <https://doi.org/10.1038/nnano.2010.29>
- [38] Fujiwara, T., Ritchie, K., Murakoshi, H., Jacobson, K., Kusumi, A. Phospholipids undergo hop diffusion in compartmentalized cell membrane. *J. Cell Biol.* 157, 1071-1082 (2002). <https://doi.org/10.1083/jcb.200202050>
- [39] Goksu, E. I., Vanegas, J. M., Blanchette, C. D., Lin, W. C., Longo, M. L. AFM for structure and dynamics of biomembranes. *Biochim. Biophys. Acta* 1788, 254-266 (2009). <https://doi.org/10.1016/j.bbamem.2008.08.021>
- [40] Sanganna Gari, R. R., Montalvo-Acosta, J. J., Heath, G. R., Jiang, Y., Gao, X., Nimigeon, C. M., et al. Correlation of membrane protein conformational and functional dynamics. *Nat. Commun.* 12, 4363 (2021). <https://doi.org/10.1038/s41467-021-24660-1>
- [41] Touhami, A., Jericho, M. H., Beveridge, T. J. Atomic force microscopy of cell growth and division in *Staphylococcus aureus*. *J. Bacteriol.* 186, 3286-3295 (2004). <https://doi.org/10.1128/JB.186.11.3286-3295.2004>
- [42] Matthews, H. K., Ganguli, S., Plak, K., Taubenberger, A. V., Win, Z., Williamson, M., et al. Oncogenic signaling alters cell shape and mechanics to facilitate cell division under confinement. *Dev. Cell* 52, 563-573.e3 (2020). <https://doi.org/10.1016/j.devcel.2020.01.004>
- [43] Yurtsever, A., Yoshida, T., Behjat, A. B., Araki, Y., Hanayama, R., Fukuma, T. Structural and mechanical characteristics of exosomes from osteosarcoma cells explored by 3D-atomic force microscopy. *Nanoscale* 13, 6661-6677 (2021). <https://doi.org/10.1039/D0NR09178B>
- [44] Fritz, M., Radmacher, M., Gaub, H. E. In vitro activation of human platelets triggered and probed by atomic force microscopy. *Exp. Cell Res.* 205, 187-190 (1993). <https://doi.org/10.1006/excr.1993.1074>
- [45] Liu, L., Wang, K., Liu, J., Wei, Y., Liu, W., Zhang, P., et al. Starvation effect on the morphology of microvilli in HeLa cells. *Biochem. Biophys. Res. Commun.* 514, 1238-1243 (2019). <https://doi.org/10.1016/j.bbrc.2019.05.073>
- [46] Butt, H. J., Wolff, E. K., Gould, S. A. C., Northern, B. D., Peterson, C. M., Hansma, P. K. Imaging cells with the atomic force microscope. *J. Struct. Biol.* 105, 54-61 (1990). [https://doi.org/10.1016/1047-8477\(90\)90098-W](https://doi.org/10.1016/1047-8477(90)90098-W)
- [47] Francis, L. W., Gonzalez, D., Ryder, T., Baer, K., Rees, M., White, J. O., et al. Optimized sample preparation for high-resolution AFM characterization of fixed human cells. *J. Microsc.* 240, 111-121 (2010). <https://doi.org/10.1111/j.1365-2818.2010.03392.x>

- [48] Kodera, N., Yamamoto, D., Ishikawa, R., Ando, T. Video imaging of walking myosin V by high-speed atomic force microscopy. *Nature* 468, 72-76 (2010). <https://doi.org/10.1038/nature09450>
- [49] Uchihashi, T., Ganser, C. Recent advances in bioimaging with high-speed atomic force microscopy. *Biophys. Rev.* 12, 363-369 (2020). <https://doi.org/10.1007/s12551-020-00670-z>
- [50] Casuso, I., Redondo-Morata, L., Rico, F. Biological physics by high-speed atomic force microscopy. *Philos. Trans. A Math. Phys. Eng. Sci.* 378, 20190604 (2020). <https://doi.org/10.1098/rsta.2019.0604>
- [51] Lindblom, G., Orädd, G. Lipid lateral diffusion and membrane heterogeneity. *Biochim. Biophys. Acta* 1788, 234-244 (2009). <https://doi.org/10.1016/j.bbamem.2008.08.016>
- [52] Chung, J. K., Lee, Y. K., Denson, J. P., Gillette, W. K., Alvarez, S., Stephen, A. G., et al. K-Ras4B remains monomeric on membranes over a wide range of surface densities and lipid compositions. *Biophys. J.* 114, 137-145 (2018). <https://doi.org/10.1016/j.bpj.2017.10.042>
- [53] Ramadurai, S., Holt, A., Krasnikov, V., van den Bogaart, G., Killian, J. A., Poolman, B. Lateral diffusion of membrane proteins. *J. Am. Chem. Soc.* 131, 12650-12656 (2009). <https://doi.org/10.1021/ja902853g>
- [54] Rong, G., Reinhard, B. M. Monitoring the size and lateral dynamics of ErbB1 enriched membrane domains through live cell plasmon coupling microscopy. *PLoS One* 7, e34175 (2012). <https://doi.org/10.1371/journal.pone.0034175>
- [55] Schütte, O. M., Mey, I., Enderlein, J., Savić, F., Geil, B., Janshoff, A., et al. Size and mobility of lipid domains tuned by geometrical constraints. *Proc. Natl. Acad. Sci. U.S.A.* 114, E6064-E6071 (2017). <https://doi.org/10.1073/pnas.1704199114>
- [56] Przybylo, M., Sýkora, J., Humpolíčková, J., Benda, A., Zan, A., Hof, M. Lipid diffusion in giant unilamellar vesicles is more than 2 times faster than in supported phospholipid bilayers under identical conditions. *Langmuir* 22, 9096-9099 (2006). <https://doi.org/10.1021/la061934p>
- [57] Gaul, V., Lopez, S. G., Lentz, B. R., Moran, N., Forster, R. J., Keyes, T. E. The lateral diffusion and fibrinogen induced clustering of platelet integrin α IIb β 3 reconstituted into physiologically mimetic GUVs. *Integr. Biol. (Camb)* 7, 402-411 (2015). <https://doi.org/10.1039/c5ib00003c>
- [58] Frick, M., Schmidt, K., Nichols, B. J. Modulation of lateral diffusion in the plasma membrane by protein density. *Curr. Biol.* 17, 462-467 (2007). <https://doi.org/10.1016/j.cub.2007.01.069>
- [59] Saffman, P. G., Delbrück, M. Brownian motion in biological membranes. *Proc. Natl. Acad. Sci. U.S.A.* 72, 3111-3113 (1975). <https://doi.org/10.1073/pnas.72.8.3111>
- [60] Javanainen, M., Martinez-Seara, H., Metzler, R., Vattulainen, I. Diffusion of integral membrane proteins in protein-rich membranes. *J. Phys. Chem. Lett.* 8, 4308-4313 (2017). <https://doi.org/10.1021/acs.jpcllett.7b01758>
- [61] Hall, D., Hoshino, M. Effects of macromolecular crowding on intracellular diffusion from a single particle perspective. *Biophys. Rev.* 2, 39-53 (2010). <https://doi.org/10.1007/s12551-010-0029-0>
- [62] Saxton, M. J. Lateral diffusion in an archipelago. The effect of mobile obstacles. *Biophys. J.* 52, 989-997 (1987). [https://doi.org/10.1016/S0006-3495\(87\)83291-5](https://doi.org/10.1016/S0006-3495(87)83291-5)
- [63] Bussell, S. J., Koch, D. L., Hammer, D. A. Effect of hydrodynamic interactions on the diffusion of integral membrane proteins: Tracer diffusion in organelle and reconstituted membranes. *Biophys. J.* 68, 1828-1835 (1995). [https://doi.org/10.1016/S0006-3495\(95\)80359-0](https://doi.org/10.1016/S0006-3495(95)80359-0)
- [64] Ando, T. Directly watching biomolecules in action by high-speed atomic force microscopy. *Biophys. Rev.* 9, 421-429 (2017). <https://doi.org/10.1007/s12551-017-0281-7>
- [65] Hall, D. Analysis and interpretation of two-dimensional single-particle tracking microscopy measurements: Effect of local surface roughness. *Anal. Biochem.* 377, 24-32 (2008). <https://doi.org/10.1016/j.ab.2008.02.019>
- [66] Hall, D. Effect of heterogeneity on the characterization of cell membrane compartments: I. Uniform size and permeability. *Anal. Biochem.* 398, 230-244 (2010). <https://doi.org/10.1016/j.ab.2009.11.033>
- [67] Meijering, E., Dzyubachyk, O., Smal, I. Methods for cell and particle tracking. *Methods Enzymol.* 504, 183-200 (2012). <https://doi.org/10.1016/B978-0-12-391857-4.00009-4>
- [68] Drake, B., Prater, C. B., Weisenhorn, A. L., Gould, S. A. C., Albrecht, T. R., Quate, C. F., et al. Imaging crystals, polymers, and processes in water with the atomic force microscope. *Science* 243, 1586-1589 (1989). <https://doi.org/10.1126/science.2928794>
- [69] Dufrêne, Y. F., Viljoen, A., Mignolet, J., Mathelié-Guinlet, M. AFM in cellular and molecular microbiology. *Cell. Microbiol.* e13324 (2021). <https://doi.org/10.1111/cmi.13324>
- [70] Müller, D. J., Engel, A., Matthey, U., Meier, T., Dimroth, P., Suda, K. Observing membrane protein diffusion at subnanometer resolution. *J. Mol. Biol.* 327, 925-930 (2003). [https://doi.org/10.1016/S0022-2836\(03\)00206-7](https://doi.org/10.1016/S0022-2836(03)00206-7)
- [71] Casuso, I., Sens, P., Rico, F., Scheuring, S. Experimental evidence for membrane-mediated protein-protein interaction. *Biophys. J.* 99, L47-L49 (2010). <https://doi.org/10.1016/j.bpj.2010.07.028>
- [72] Nicolson, G. L. The fluid—Mosaic model of membrane structure: Still relevant to understanding the structure, function and dynamics of biological membranes after more than 40 years. *Biochim. Biophys. Acta* 1838, 1451-1466 (2014). <https://doi.org/10.1016/j.bbamem.2013.10.019>

- [73] van Deventer, S., Arp, A. B., van Spriel, A. B. Dynamic plasma membrane organization: A complex symphony. *Trends Cell Biol.* 31, 119-129 (2021). <https://doi.org/10.1016/j.tcb.2020.11.004>
- [74] Amyot, R., Flechsig, H. BioAFMviewer: An interactive interface for simulated AFM scanning of biomolecular structures and dynamics. *PLoS Comput. Biol.* 16, e1008444 (2020). <https://doi.org/10.1371/journal.pcbi.1008444>
- [75] Heath, G. R., Kots, E., Robertson, J. L., Lansky, S., Khelashvili, G., Weinstein, H., et al. Localization atomic force microscopy. *Nature* 594, 385-390 (2021). <https://doi.org/10.1038/s41586-021-03551-x>
- [76] Bevington, P. R., Robinson, D. K. *Data reduction and error analysis* (McGraw Hill, New York, 2003).
- [77] Ridolfi, A., Caselli, L., Montis, C., Mangiapia, G., Berti, D., Brucale, M., et al. Gold nanoparticles interacting with synthetic lipid rafts: an AFM investigation. *J. Microsc.* 280, 194-203 (2020). <https://doi.org/10.1111/jmi.12910>
- [78] Raulf, A., Spahn, C. K., Zessin, P. J. M., Finan, K., Bernhardt, S., Heckel, A., et al. Click chemistry facilitates direct labelling and super-resolution imaging of nucleic acids and proteins. *RSC Adv.* 4, 30462-30466 (2014). <https://doi.org/10.1039/C4RA01027B>
- [79] Yano, Y., Matsuzaki, K. Live-cell imaging of membrane proteins by a coiled-coil labeling method—Principles and applications. *Biochim. Biophys. Acta Biomembr.* 1861, 1011-1017 (2019). <https://doi.org/10.1016/j.bbamem.2019.02.009>
- [80] Henderson, R. M., Edwardson, J. M., Geisse, N. A., Saslowsky, D. E. Lipid rafts: Feeling is believing. *News Physiol. Sci.* 19, 39-43 (2004). <https://doi.org/10.1152/nips.01505.2003>
- [81] Borisy, G. G., Svitkina, T. M. Actin machinery: Pushing the envelope. *Curr. Opin. Cell Biol.* 12, 104-112 (2000). [https://doi.org/10.1016/S0955-0674\(99\)00063-0](https://doi.org/10.1016/S0955-0674(99)00063-0)
- [82] Liang, K., Wei, L., Chen, L. Exocytosis, endocytosis, and their coupling in excitable cells. *Front. Mol. Neurosci.* 10, 109 (2017). <https://doi.org/10.3389/fnmol.2017.00109>
- [83] Vesperini, D., Montalvo, G., Qu, B., Lautenschläger, F. Characterization of immune cell migration using microfabrication. *Biophys. Rev.* 13, 185-202 (2021). <https://doi.org/10.1007/s12551-021-00787-9>
- [84] Al-Jumaa, M., Hallett, M. B., Dewitt, S. Cell surface topography controls phagocytosis and cell spreading: The membrane reservoir in neutrophils. *Biochim. Biophys. Acta Mol. Cell Res.* 1867, 118832 (2020). <https://doi.org/10.1016/j.bbamer.2020.118832>
- [85] Fenteany, G., Zhu, S. Small-molecule inhibitors of actin dynamics and cell motility. *Curr. Top. Med. Chem.* 3, 593-616 (2003). <https://doi.org/10.2174/1568026033452348>
- [86] Koç, M. M., Ragkousis, G. E. AFM induced diffusion of large scale mobile HOPG defects. *Appl. Nanosci.* 9, 1459-1468 (2019). <https://doi.org/10.1007/s13204-018-0929-z>
- [87] Ala-Nissila, T., Ferrando, R., Ying, S. C. Collective and single particle diffusion on surfaces. *Adv. Phys.* 51, 949-1078 (2002). <https://doi.org/10.1080/00018730110107902>
- [88] Florin, E. L., Moy, V. T., Gaub, H. E. Adhesion forces between individual ligand-receptor pairs. *Science* 264, 415-417 (1994). <https://doi.org/10.1126/science.8153628>
- [89] Boscoboinik, J. A., Kohlmeyer, R. R., Chen, J., Tysoc, W. T. Efficient transport of gold atoms with a scanning tunneling microscopy tip and a linker molecule. *Langmuir* 27, 9337-9344 (2011). <https://doi.org/10.1021/la202134a>
- [90] Melzak, K. A., Moreno-Flores, S., Yu, K., Kizhakkedathu, J., Toca-Herrera, J. L. Rationalized approach to the determination of contact point in force–distance curves: Application to polymer brushes in salt solutions and in water. *Microsc. Res. Tech.* 73, 959-964 (2010). <https://doi.org/10.1002/jemt.20851>
- [91] Fan, T. H., Fedorov, A. G. Analysis of hydrodynamic interactions during AFM imaging of biological membranes. *Langmuir* 19, 1347-1356 (2003). <https://doi.org/10.1021/la026328i>
- [92] Liang, Y., Hilal, N., Langston, P., Starov, V. Interaction forces between colloidal particles in liquid: Theory and experiment. *Adv. Colloid Interface Sci.* 134-135, 151-166 (2007). <https://doi.org/10.1016/j.cis.2007.04.003>
- [93] Phillips, R., Kondev, J., Theriot, J., Garcia, H. G., Orme, N. *Physical biology of the cell* (Garland Science, New York, 2012). <https://doi.org/10.1201/9781134111589>
- [94] Hecht, F. M., Rheinlaender, J., Schierbaum, N., Goldmann, W. H., Fabry, B., Schäffer, T. E. Imaging viscoelastic properties of live cells by AFM: Power-law rheology on the nanoscale. *Soft Matter* 11, 4584-4591 (2015). <https://doi.org/10.1039/C4SM02718C>
- [95] Penedo, M., Shirokawa, T., Alam, M. S., Miyazawa, K., Ichikawa, T., Okano, N., et al. Cell penetration efficiency analysis of different atomic force microscopy nanoneedles into living cells. *Sci. Rep.* 11, 7756 (2021). <https://doi.org/10.1038/s41598-021-87319-3>
- [96] Kwon, E. Y., Kim, Y. T., Kim, D. E. Investigation of penetration force of living cell using an atomic force microscope. *J. Mech. Sci. Technol.* 23, 1932-1938 (2009). <https://doi.org/10.1007/s12206-009-0508-z>
- [97] Hall, D. Kinetic models describing biomolecular interactions at surfaces. *Handbook of Surface Plasmon Resonance*, pp. 81-122 (2008).

